Granular avalanches on the Moon: Mass-wasting conditions, processes, and features

B. P. Kokelaar, R. S. Bahia, K. H. Joy, S. Viroulet, J. M. N. T. Gray

AGU PUBLICATIONS

JGR

Journal of Geophysical Research: Planets

RESEARCH ARTICLE
10.1002/2017JE005320

Key Points:
- Recent LROC imaging of the lunar surface facilitates moderately detailed sedimentological analysis and comparisons with laboratory granular flow experiments
- Three end-member types of debris flow deposit are identified having formed without influence of atmosphere or liquid, and two are similar to types seen on Earth
- Deposits of long-runout granular erosion-deposition waves are recognized for the first time in nature and formed on repose slopes dominantly of fine regolith

Supporting Information:
- Supporting Information S1

Correspondence to:
K. H. Joy,
katherine.joy@manchester.ac.uk

Citation:
Kokelaar, B. P., R. S. Bahia, K. H. Joy, S. Viroulet, and J. M. N. T. Gray (2017), Granular avalanches on the Moon: Mass-wasting conditions, processes, and features, *J. Geophys. Res. Planets*, *122*, 1893–1925, doi:10.1002/2017JE005320.

Received 5 APR 2017
Accepted 25 JUL 2017
Accepted article online 7 AUG 2017
Published online 21 SEP 2017

Granular avalanches on the Moon: Mass-wasting conditions, processes, and features

B. P. Kokelaar[1], R. S. Bahia[2], K. H. Joy[2], S. Viroulet[3,4], and J. M. N. T. Gray[3]

[1]School of Environmental Sciences, University of Liverpool, Liverpool, UK, [2]School of Earth and Environmental Sciences, University of Manchester, Manchester, UK, [3]School of Mathematics, University of Manchester, Manchester, UK, [4]Now at Institut de Physique du Globe de Paris, Sorbonne Paris Cité, Paris, France

Abstract Seven lunar crater sites of granular avalanches are studied utilizing high-resolution images (0.42–1.3 m/pixel) from the Lunar Reconnaissance Orbiter Camera; one, in Kepler crater, is examined in detail. All the sites are slopes of debris extensively aggraded by frictional freezing at their dynamic angle of repose, four in craters formed in basaltic mare and three in the anorthositic highlands. Diverse styles of mass wasting occur, and three types of dry-debris flow deposit are recognized: (1) multiple channel-and-lobe type, with coarse-grained levees and lobate terminations that impound finer debris, (2) single-surge polylobate type, with subparallel arrays of lobes and fingers with segregated coarse-grained margins, and (3) multiple-ribbon type, with tracks reflecting reworked substrate, minor levees, and no coarse terminations. The latter type results from propagation of granular erosion-deposition waves down slopes dominantly of fine regolith, and it is the first recognized natural example. Dimensions, architectures, and granular segregation styles of the two coarse-grained deposit types are like those formed in natural and experimental avalanches on Earth, although the timescale of motion differs due to the reduced gravity. Influences of reduced gravity and fine-grained regolith on dynamics of granular flow and deposition appear slight, but we distinguish, for the first time, extensive remobilization of coarse talus by inundation with finer debris. The (few) sites show no clear difference attributable to the contrasting mare basalt and highland megaregolith host rocks and their fragmentation. This lunar study offers a benchmarking of deposit types that can be attributed to formation without influence of liquid or gas.

Plain Language Summary The Moon is a large-scale natural laboratory where surface processes occur without the presence of atmosphere or liquid, making it a relatively accessible analogue of other airless rocky bodies in our Solar System. Recently very high resolution images (~0.5 meters-per-pixel) of the Moon have been taken from orbit, allowing for our new study of lunar avalanches to better understand planetary mass wasting processes. Our work focuses on seven impact crater sites from across the Moon. We compared our findings with avalanche deposits found on Earth, and with the results from laboratory experiments, to detect differences and understand lunar processes. We find that reduced gravity on the Moon does not affect the morphology of the avalanche deposits, although the timescale of motion is longer on the Moon. We identify a new type of avalanche deposit that has never been seen naturally 'in the field' on Earth, and that has only recently been discovered and understood from small-scale laboratory experiments. This new type of flow produces long and narrow ribbons of material formed from granular erosion-deposition waves that propagate down slopes dominated by fine-grained particles. The extremely long runout of flows on the Moon results from the existence of very long slopes close to the material angle of stable repose, a situation that does not occur onEarth. Our work establishes the variety of flow deposit types that can arise where there is no atmosphere or liquid. The study has important implications for granular avalanche processes on other planets, such as Mars.

1. Introduction

Avalanches degrade and obscure the impact crater record of bombardment of the rocky planets and large asteroids in our Solar System [e.g., *Melosh*, 1986]. Understanding the surfaces of these bodies is important for recognition of their underlying geology and their evolution through deep time. The Moon is particularly important to study; it probably originated from the same giant impact event that formed the Earth [*Canup and Asphaug*, 2001; *Canup*, 2012], and it records a history of bombardment that also affected Earth throughout the past 4.5 Ga [*National Research Council (NRC)*], 2007; *Joy et al*., 2016]. Further, it is a natural laboratory where geomorphic degradation occurs with no significant influence by liquid water or atmosphere, and, thus, it constrains inferences of such involvement on other planets [*Stöffler et al*., 2006; *NRC*, 2007]. The

Table 1. Dry Granular Mass-Wasting Processes and Features on the Moon

Process Term	Movement Behavior	Slope Failure	Deposit Features
Debris fall	Particles detach from a steep free surface in groups, then bounce, roll, and may break independently; particle motion is rapid and momentum dominates; fines may segregate to form a flow	Single or irregularly retrogressive; typically unsteady; steep rock slopes locally shattered by impacts	Longitudinal size grading; largest grains travel farthest, as in scree; large boulders may reach far beyond main deposit pile; fines tend to form cone or apron apex, or streaky veneers
Debris slide	Particles move en masse, as a slab on a basal detachment; basal friction dominates	Headwall detachment scarp curves into basal detachment with lateral dislocations; single or retrogressive	Retains initial slab "stratigraphy"; may have slight compression or extension features, with or without deformed edges
Debris slump	Moves like debris slide, but slab deforms internally forming shears, folds and/or stacked slices; basal and internal friction dominate	Headwall detachment scarp curves into basal detachment with lateral dislocations; single or retrogressive	Retains some initial stratigraphy but deformed in folds and/or slice stacks during progressive pileup
Debris flow	Slightly dilated particle mass shears throughout (may form free-surface raft); diverse particles susceptible to vertical and longitudinal segregation during transport; self-channelization common; thin flows develop waves; flow can be erosive, increasing bulk, and deposits aggrade progressively; interparticle friction dominates	Single or retrogressive, typically unsteady, with or without headwall scarp; commonly transformed downstream from falls, slides, and slumps; waves on erodible slopes at repose angle advance and leave trail by reworking the slope deposit	Tend to form fingers or lobes on moderate slopes; may form fan on low slopes; marginal levees and drained channels typical behind bulbous front; breached lobes recording flow surges are common; deposition progressive; grain size segregation typical; ribbon-like reworking trails can form on regolith slope at angle of repose
Debris creep	Particulate mass shears slowly and incrementally; interparticle friction dominates	Minor dislocations and mixing caused by ground shaking and impacts	Tend to form extensive areas of irregular, low-amplitude transverse ridges

complete surface of the Moon has only recently become accessible to moderately detailed sedimentological scrutiny, owing to the fine resolution, to 0.5 m/pixel, of recent satellite imagery.

Mass wasting is the bulk movement of rock debris and/or soil downslope due to gravity [e.g., *Jain*, 2014]. The processes occur widely on Earth, mostly on steep slopes, both subaerially and under water [e.g., *Moore et al*., 1994; *Deplus et al*., 2001; *Wolman and Gerson*, 2007; *Corsini et al*., 2009; *Parker et al*., 2011]. On the Moon mass wasting principally occurs on slopes that originally formed by impact cratering and it differs from Earth in commonly involving some proportion of fine-grained (powder-like) regolith and no liquid water or atmospheric gas [*Pike*, 1971; *Melosh*, 1986; *Bart*, 2007]. Also, experiments suggest that the relatively low lunar gravity (0.16 *g*) can slightly decrease the dynamic angle of repose, reflected in the free-surface slope formed in frictional freezing from granular flow [*Kleinhans et al*., 2011], although numerical modeling finds a negligible effect [*Chen et al*., 2015].

The majority of lunar impact craters were formed more than 3.8 billion (10^9) years ago, and they vary greatly in size. All initially had steep walls ($\geq 30^o$) that soon degraded gravitationally, with or without seismic shaking, and many formed with concentric fault scarps susceptible to collapse; large impact craters, $>$15 km in diameter, typically developed a central peak [*Wilhelms*, 1987; *Melosh and Ivanov*, 1999; *Stöffler et al*., 2006]. Such ancient craters have been heavily degraded by ongoing bombardment and regolith development, and now they rarely have slopes $>35°$ [*Pike*, 1967; *Melosh*, 1984; *Kreslavsky and Head*, 2016]. Scars from slope failures and deposits recording mass wasting are ubiquitous and have long been recognized in the younger (i.e., $<$1 Ga) well-preserved "fresh" craters [*Howard*, 1973; *Melosh*, 1986]. Unlike on Earth and Mars, mass-wasting features on the Moon can remain practically pristine for hundreds of millions of years owing to the absence of erosion, although bombardment and cover by ejecta tend to degrade older examples [e.g., *Basilevsky et al*., 2013, 2014].

It has only recently become possible to study the global extent of lunar mass wasting in detail [e.g., *Kumar et al*., 2013; *Xiao et al*., 2013], using satellite images that have submeter spatial scale resolution, from NASA's Lunar Reconnaissance Orbiter Camera Narrow Angle Camera (LROC-NAC) [*Robinson et al*., 2010].

Studies of lunar mass wastage deposits have led to inference of debris movement processes akin to those on Earth [e.g., *Xiao et al*., 2013], because most lunar features appear to have closely similar terrestrial counterparts. However, the terminology applied to Moon phenomena has tended to be inconsistent with modern sedimentological use, vague or incompletely justified. Table 1 shows the simple scheme we use

Table 2. Craters and Deposits Studied

Crater with its Diameter (km)	Latitude	Longitude	Target Rock	Runout (km)	Deposit Midslope Angle and Range (deg)	Thickness Average and Range (m)	Extent (km^2)	Maximum Volume[a] (m^3)
Kepler (31)	8.13°N	37.98°W	Mare basalt	2.50	33 to 32 (36 to 9)[b]	1.88 (0.20 to 8.00)	3.55	Multiple small
Gambart B (11)	2.15°N	11.35°W	Mare basalt	2.93	32 to 29 (38 to 27)	1.15 (0.96 to 2.24)	0.24	0.27×10^6
Bessel (16)	21.8°N	17.9°E	Mare basalt	1.86	31.5 (35 to 31.5)	7.14 (4.13 to 12.3)	2.46	15.2×10^6
Censorinus (3.8)	0.47°S	32.73°E	Mare basalt	2.18	32 (34 to 25)	11.02 (10.12 to 13.49)[c]	0.44[c]	4.7×10^{6c}
Riccioli CA (14.2)	0.58°N	73.01°W	Highlands (Orientale basin distal ejecta blanket)	1.77	34 (34.5 to 27)	2.77 (2.38 to 11.12)	0.67	1.65×10^6
Virtanen F (11.8)	15.76°N	177.31°E	Highlands – farside central highlands megaregolith	4.58	32 (34.5 to 27.5)	Widely no measurable shadows	0.94	Multiple very small
Tralles A (18)	27.44°N	46.97°E	Highlands (Crisium basin ejecta blanket)	6.11	32 (32 to 19)	1.00 (0.58 to 1.96) (Widely no measurable shadows)	1.55	Multiple small

[a]Volumes are approximate maxima and are the sum of volumes in measured segments (not simply overall average thickness × areal extent). The deposit volumes must significantly exceed any volumes of dense rock that collapsed at the source, according to the loose-material packing density.
[b]Slope ranges are from 13 profiles that include low slopes.
[c]Calculation based on upper set of slope foot deposits (see Figure 11).

concerning granular mass-movement processes on the Moon and their key features. This simplicity does not readily apply to all Earth phenomena, not least because many terrestrial flows involve or occur under water, and some include significant cohesive clay minerals. The term "avalanche" would be applicable to any one or combination of the phenomena, excluding creep. In both lunar and terrestrial contexts, so-called "debris avalanches" usually entail a range of processes and evolutions from one to another.

In this paper we use well-illuminated LROC-NAC images (supporting information Table S1) to describe and interpret scars and deposits formed by mass wasting within four case study craters that formed in lunar maria and three that formed in the lunar highlands, all in broadly equatorial (nonpolar) latitudes. Table 2 gives the crater locations and provides details of each site, and Figure S6 shows these craters in the global lunar context. We present a thorough survey and detailed interpretation of the various features exposed in one narrow segment of the wall of Kepler crater, formed in a mare basalt target rock. Then we briefly examine the other craters, to consider some additional features and to explore whether mass wasting in mare settings differs significantly from that in highlands target rocks. We make comparisons with terrestrial counterparts and results from laboratory experiments (Figures S1–S5), to distinguish differences and to understand the lunar processes. We consider the effects of reduced gravity on lunar material movement, as well as the influence of the abundant fine rock "powder" that characterizes the lunar regolith. Finally, we highlight three previously unrecognized phenomena: (1) remobilization of stable coarse talus by inundation with finer debris; (2) development of veils of finer-grained debris around the coarse-grained peripheries of some segregated flow deposits; and (3) occurrence of long-runout erosion-deposition waves.

1.1. Mass Wasting: A Brief Review

On the Moon there are deposits we interpret as recording rapid collisional debris falls, dense frictional debris flows, slides, slumps, and creep (Table 1), all formed there without influence of interstitial liquid or gas. Deposition from debris falls and flows is sensitive to the angle of repose of the granular material, which is a function of intergranular friction and varies mainly with grain size, shape, and density [*Train*, 1958; *Carrigy*, 1970; *Zhou et al*., 2002]. Dense frictional flows involving a mixture of grain sizes (polydisperse) tend spontaneously to segregate and deposit relatively coarse marginal levees with finer-grained material in between (Figures S1 and S2). The particle size

segregation occurs dominantly by so-called kinetic sieving and squeeze expulsion; in a shearing (slightly dilated) dispersion small particles fall between larger ones and large ones are "levered" upward [*Savage and Lun*, 1988; *Takahashi et al*., 1992; *Vallance and Savage*, 2000; *Gray and Thornton*, 2005; *Gray and Kokelaar*, 2010]. Thus, a polydisperse flow tends to develop a coarse-grained upper part, which, traveling fastest, shears to the flow front. There it presents relatively high frictional resistance to flow and is advected laterally and then deposited from the back of the flow head to form lateral levees; finer grains tend to be deposited to form a channel lining with relatively low friction. This segregation that forms a channel conduit for following material constitutes a self-organized feedback that counters flow spreading and facilitates minimum frictional resistance to flow [*Gray and Thornton*, 2005; *Johnson et al*., 2012; *Kokelaar et al*., 2014; *Baker et al*., 2016a]. Flow fronts that are continuously fed via the channel conduit may continue to deposit across slopes considerably less steep than the material angles of repose before complete frictional freezing; momentum and low friction can permit some ascent of adverse slopes. On the other hand, flows starved of material supply may reach their maximum runout and stop on continuous-gradient repose slopes. It is well known that many large-volume flows of debris on Earth extend surprisingly large distances on low and adverse slopes, but this is not clearly apparent on the fluid-free Moon, where debris flows must have been dry and extensive low-slope flow deposits seem rare and related to impacts [*Howard*, 1973; *Legros*, 2002]. We discuss the issues concerning fluid-moderated flow further in section 5.4, as they bear on other planetary bodies.

The development of a frictionally resistive flow front with more mobile debris behind results in the frontal region, both of the active flow head and then its ultimate deposit, becoming slightly bulbous in profile and lobate or finger-like in plan view [*Pouliquen et al*., 1997; *Pouliquen and Vallance*, 1999; *Woodhouse et al*., 2012; *Baker et al*., 2016b]. For descriptive simplicity here we designate "lobes" as having length:width ratio $\leq$1.5 and "fingers" $>$1.5.

Granular flows can spontaneously develop quasiperiodic roll waves [*Forterre and Pouliquen*, 2003; *Forterre*, 2006; *Gray and Edwards*, 2014; *Razis et al*., 2014; *Edwards and Gray*, 2015], or erosion-deposition waves [*Edwards and Gray*, 2015; *Edwards et al*., 2017], wherein the downslope wave speed is faster than the net material flow and the front advances in mass flux surges as the waves arrive there. For dense granular flows, roll waves develop when the Froude number $Fr = |\overline{\boldsymbol{u}}|/\sqrt{ghcos\,\theta}$ is greater than 2/3, where $|\overline{\boldsymbol{u}}|$ is the depth-averaged flow speed, g is the constant of gravitational acceleration, h is the flow thickness, and θ is the slope inclination.

Erosion-deposition waves can develop in flows with very low Froude numbers and are typified by material being completely stopped between the wave crests [*Edwards and Gray*, 2015]. Debris is alternately erosionally incorporated into each following wave and then deposited from its rear. Waves may catch up with predecessors and become bigger but only up to a critical limit [*Razis et al*., 2014]. Additionally, solitary granular waves can propagate down repose-angled slopes of erodible material, with the cycle of erosion-deposition continuously involving preexisting slope material such that the initial singular release acts to rework the slope far beyond its own material extent [*Edwards et al*., 2017] (Figure S3). Thus, although continuous lateral levees and long fingers (up to several kilometers) typically record sustained material supply, solitary granular waves originating from a limited-mass release and moving steadily down erodible repose-angled substrate also can form continuous leveed channels. These latter features, however, are restricted to repose slopes, are distinctly parallel sided, and tend to be relatively subdued, because the cross-sectional area of the constructed levees must be the same as that of the eroded channel, i.e., there is no net material loss or gain due to the passing wave, just redistribution. We invoke this latter mechanism, for the first time, for some lunar features, where the widespread availability of erodible fine material (regolith) at or close to its angle of repose seems the key control of occurrence. Reduced gravity serves to increase the timescale for the motion by reducing the flow velocity, but otherwise flows and their deposits do not change their morphology. This result is shown explicitly in section 4.

In contrast to dense frictional debris flow, particle motion in debris fall is dominated by momentum and collisions during bouncing and rolling [*Varnes*, 1978]. Because of their greater momentum, large particles tend to travel farther than small ones and debris fall deposits typically are longitudinally graded, with the large particles concentrated near the slope base and especially massive ones commonly run out far beyond this. Examples in the lunar craters illustrate this especially well, since bounce and roll tracks can be well

preserved in the regolith. In debris fall, finer material typically segregates and lags behind on slopes overpassed by coarser debris, forming nonuniform flows that tend to deposit in streaks.

Slides and slumps move according to slope loading and friction on the basal detachment, and they may, primarily according to slope, transform into (free-surface) debris flows. Whereas on Earth slides and slumps commonly initiate under conditions of increased pore fluid pressure, typically of water, this cannot apply on the Moon. Mass movement by creep generally involves slight and generally infrequent disturbances of intergranular friction, on the Moon mainly due to ground shaking from impact events or internally driven moonquakes [*Houston et al*., 1973; *Kumar et al*., 2016].

All of the primary flow types discussed above can interact with and cause mobilization of existing substrate, broadly considered as erosion. Thus, for example, in energetic reaches of debris flows and falls material can be added to the moving mass, referred to as bulking, with consequences for the resulting dynamics of motion and deposition [e.g., *Iverson et al*., 2011; *Frank et al*., 2015]. Incorporation of fine-grained material in otherwise coarse debris is known to reduce effective friction (see below) and hence increase mobility, and in this paper we consider the importance of the virtually ubiquitous fine surficial regolith in influencing flow type and runout on the Moon (and presumably other dry airless bodies).

1.2. Lunar Crater Slopes

The slopes studied here originated from the dynamics of impact cratering, most of which occurred in deep time such that they now inevitably reflect modifications by protracted mass wasting with ongoing impact ejecta emplacement and micrometeorite bombardment. Initial impact-related excavation and subsidence typically produce inner crater slopes that are so steep that they fail immediately, so most craters contain accumulations of fault blocks, terraces, and smaller debris reflecting this catastrophic mass wasting [*Melosh and Ivanov*, 1999]. The lower parts of crater wall slopes widely accumulate debris that has aggraded at the dynamic angle(s) of repose (see section 1.3 below), while upper slopes of younger craters expose degraded cliffs of bedrock with intervening alcoves or gullies [*Bart*, 2007; *Kumar et al*., 2013]. The ancient slopes strewn with granular debris at or near its angle of stable repose are susceptible to material overpassing (little or no deposition), so avalanche trails commonly traverse them extensively if not entirely and the slope base is to an extent buttressed by deposits from flows arrested there or a little beyond. Failure of marginally stable slopes may be triggered directly by impact(s) or by seismic shaking (moonquakes) resulting from impacts elsewhere, internal geodynamic processes (tides and shrinkage) or regional tectonic activity, or from thermal expansion and contraction [*Melosh*, 1984; *Fassett and Thomson*, 2014; *Molaro and Byrne*, 2012; *Schultz and Gault*, 1976; *Watters et al*., 2012; *Kumar et al*., 2016; *Schmitt et al*., 2017]. Impacts by micrometeorites (0.1 to 2 mm in size) also degrade rock surfaces and may cause detachment of surface grains that conceivably could trigger small flows [*Soderblom*, 1970; *Hörz et al*., 1971; *Basilevsky et al*., 2013; *Bandfield et al*., 2014].

1.3. Granular-Slope Stability

The steepest stable slope that is achievable by the free surface of a pile of grains is its static angle of repose, which varies according to the grain size, grain size range, grain packing, grain shape, and grain surface roughness of the material [*Train*, 1958; *Carrigy*, 1970; *Zhou et al*., 2002; *Pohlman et al*., 2006]. Interstitial fluid (e.g., water, gas, and dusty gas) can modify granular deposit stability, but this is not relevant for the atmosphere-free Moon. In general, irregular and angular, coarse rock fragments ($>$2 mm; i.e., coarser than coarse sand) have a steeper static angle of repose than finer sand and/or rounded fragments, primarily because the intergranular friction is greater; in natural systems there typically is a range of stable repose angles. The free-surface slope of grains deposited from a flow, reflecting frictional freezing, is the dynamic angle of repose, which is slightly less than its static counterpart [*Pouliquen*, 1999; *Jop et al*., 2006]. Momentum and reduced friction that is related to dilation allow a granular flow to extend to form slopes less than the static angle of repose, especially on erodible substrates [*Mangeney et al*., 2010].

On the Moon, theoretically, differences in repose angle might reflect differing fragmentation of the crater source rocks, for example, mare basalt lava flows versus highland anorthosite (see below), as well as differing involvement (0–100%) of unconsolidated regolith. A distinctive feature of the Moon, absent on Earth, is the almost ubiquitous surface occurrence of fine-grained, powder-like, surficial regolith [*Shorthill*, 1970; *McKay et al*., 1974, 1991; *Mendell and Low*, 1974, 1975; *Oberbeck et al*., 1975; *Lucey et al*., 2006] and highly fractured impact crater wall and ejecta deposits with a wide range of particle size. On Earth, at low abundances,

admixed fines tend to act as a "lubricant" between large particles [*Hsü*, 1975; *GDR Midi*, 2004; *Kokelaar et al*., 2014], whereas on the Moon it has been suggested that the angularity of regolith grains may enhance stability [*Wagner et al*., 2013].

On the lunar surface an adhesive force for particles <50 μm, involving adsorbed molecular layers and van der Waals forces, and mediated by surface roughness, acts with gravity [*Izvekova and Popel*, 2013] and may mimic the terrestrial effects of capillary attraction (i.e., surface tension) and wet bridging [*Megens and Aizenberg*, 2003]. This could explain why the fine fraction (alone) of dry piled lunar regolith has an angle of repose of ~40°, between that of wet sand (~45°) and dry sand (~34°) [*Carrier et al*., 1991]. This might be relevant where regolith collapses retrogressively at the source of flows, forming relatively steep scars, but we recognize no evidence of this. Although fine particles can become charged and susceptible to electrostatic forces at the surface of the Moon, where a plasma forms from unimpeded solar wind [*Colwell et al*., 2007; *Popel et al*., 2013], mechanical disturbance readily overcomes any coherence of fine regolith and the forces cannot be implicated in the stopping of flows (deposition) or the dynamic angle of repose. The absence of atmosphere and relative weakness of electrostatic forces mean that particles launched from collisions in granular avalanches are likely to follow essentially ballistic trajectories. We consider whether fine particles are sprayed ballistically beyond blocky terminations of flow deposits.

1.4. Lunar Geology and Surface Processes

The lunar highlands primarily comprise variably coarse-grained anorthositic rocks (plagioclase with minor pyroxene and olivine), which, although considerably modified, confer the relatively bright albedo seen from Earth. These rocks formed between ~4.5 and 4.2 Ga and were severely influenced by bombardment in the era of basin formation prior to 3.8 Ga [*NRC*, 2007; *Stöffler et al*., 2006; *Petro and Pieters*, 2008; *Pernet-Fisher and Joy*, 2016]. The darker material of the lunar surface relates to basaltic lava flows (plagioclase and pyroxene with minor olivine and ilmenite). Partial melting in the lunar interior formed basaltic magmas that erupted and flowed into topographic lows, forming the maria, between ~3.8 and 2.5 Ga and possibly as recently as 1 Ga [*Hiesinger and Head*, 2006].

The lunar surface comprises loose rock particles, regolith, which almost completely covers the bedrock, except on steep slopes such as occur on very young crater walls [*Langevin and Arnold*, 1977; *Hörz et al*., 1991; *McKay et al*., 1991; *Lucey et al*., 2006; *Spray*, 2016]. Regolith has no counterpart on Earth, where it would be highly susceptible to erosion by wind and water. Both regolith and surface-exposed bedrock in equatorial regions of the Moon, as sampled at the Apollo and Luna mission landing sites and extending as far as ~70°N and S, are considered to be essentially dry (i.e., only tens of parts per million level hydrogen determined in Apollo samples) [*McCubbin et al*., 2015, and references therein]. However, some permanently shadowed regions of the lunar poles may contain a subsurface or disseminated ice component [*Arnold*, 1979; *Spudis et al*., 2013; *McCubbin et al*., 2015] resulting in variable physical properties [e.g., *Pitcher et al*., 2016]. Our study focuses on mass wasting on impact crater slopes occurring in dry lunar equatorial environments (Figure S6).

1.4.1. Crater Target Rock Properties

The target rock strength (i.e., whether coherent or incoherent material) will influence the resulting crater wall stability and nature of mass-wasting material. For example, impacts into the extremely ancient, heavily bombarded lunar highlands will excavate material from structurally disturbed crust overlain by multiple impact ejecta blankets, where this "megaregolith" is estimated to be up to ~10 km deep [*Hiesinger and Head*, 2006; *Spray*, 2016]. Crater wall slopes in such highland crater sites, therefore, will be formed of heterogeneous and incoherent impact ejecta. As the surface regolith is thinner on mare basalts (typically $\leq$10 m) compared with the lunar highlands deep megaregolith [*Freeman*, 1981; *Hörz et al*., 1991; *McKay et al*., 1991; *Bart et al*., 2011; *Bart*, 2014; *Spray*, 2016], small impacts into mare basalt targets will reveal crater walls with coherent layering [e.g., *Kickapoo Lunar Research Team and Kramer*, 2014] and will more easily extract and scatter fragments of previously coherent rock into the surrounding ejecta blanket [*Wilcox et al*., 2005; *Meyer*, 2011]. We consider whether the possible differences in material properties have affected mass wastage mechanics on slopes of mare basalt versus ancient highland craters.

1.4.2. Crater Wall Geological Properties

We have yet to investigate and directly sample any lunar impact crater walls, so the variability of grain size range, grain shape, and physical properties is unknown. However, photographs of steep slopes taken by the Apollo astronauts (i.e., Apollo 16: North Ray crater and Apollo 15: Hadley Rille wall) suggest that there

is a wide range of particle sizes, ranging from a large "rock" fraction on the scale of boulders up to tens of meters down to cobble- and pebble-sized material ranging down to a <10 mm "soil" fraction. Lunar regolith sampled in intercrater plains by the Apollo astronauts is dominated by poorly sorted silty sand to sandy silt, mainly <2 mm and averaging ~60 μm, with ~10–20% at <20 μm [*Carrier et al*., 1991; *McKay et al*., 1991]. These lunar "fines" dominate the mechanical properties of the lunar surface environment, creating a "fluffy," porous surficial layer (bulk density 0.8 g/cm^3) with more highly packed fabrics (bulk density: 2.1 g/cm^3) at depths of 2–3 m [*Carrier*, 1973, 2003; *McKay et al*., 1974; *Carrier et al*., 1991].

1.4.3. Landform Modification Processes

Lunar mass-wasting deposits are subject to postemplacement reworking and impact modification, and such processes usefully indicate the relative and "absolute" age. For example, regolith development on pre-Copernican aged (≤1.1 Ga) craters has obscured any detail of avalanche deposits, and, thus, our understanding of mass wastage processes is biased toward younger features and triggers. Surface-exposed boulders are gradually degraded by thermal fatigue from diurnal temperature cycles [e.g., *Delbo et al*., 2014; *Molaro et al*., 2017] and also from micrometeorite bombardment and fragmentation by more energetic impactors [*Basilevsky et al*., 2013; *Ghent et al*., 2014]. Typically, regolith formation produced on the order of ~3–5 mm of new regolith per million years at ~3.8 Ga and about 1 mm/Myr from ~3.5 Ga to the present day [*Oberbeck and Quaide*, 1968; *Quaide and Oberbeck*, 1975; *Hörz et al*., 1991]. This indicates that most lunar surface boulders larger than ~2 m are likely to become destroyed in 150–300 million years, primarily as a consequence of degradation by micrometeorite impacts [*Basilevsky et al*., 2013; *Ghent et al*., 2014]. We exploit the fact that individual boulders can now be resolved in images from the LROC-NAC to investigate the grain size distribution in a range of lunar mass wastage avalanche deposits.

2. Methods: Data Sets and Analysis

We used NASA Lunar Reconnaissance Orbiter Camera (LROC) Narrow Angle Camera (NAC) Planetary Data System released images with a spatial scale of 0.42–1.3 m/pixel (Table S1) [*Robinson et al*., 2010; *Tran et al*., 2010]. Images were map-projected using the United States Geological Survey (USGS) Map Projection Web Service (POW) image processing cloud to generate ArcMap 10.2.1 readable .cub file formats. We also used digital elevation models (DEMs), created using information from the Lunar Orbiter Laser Altimeter (LOLA) [*Smith et al*., 2010] and "Kuguya Terrain Camera DEM Merge 60N60S 512 ppd", with horizontal resolution of 59 m/pixel at the equator and ~3–4 m vertical accuracy [*Barker et al*., 2016] (see Figures S7–S13). Morphological characteristics and measures of length, slope angle and area of mass-wasting features were determined using ArcMap 10.2.1 (Table 2). These data, coupled with approximations of deposit thickness (see below), were used to estimate roughly the volumes of transported material.

2.1. Length and Slope Angle

Horizontal extents of flow deposits were found from the LROC-Wide Angle Camera (WAC) Mosaic Global 100 m/pixel data set, with ArcMap 10.2.1 used to plot source and termination coordinates and the ruler tool used to measure distance. In most instances the "source," in and around cliffs with alcoves and gullies, had no precise point location, but rather an uncertain area, so an average distance was taken from multiple (≤10) likely source area coordinates. Elevation for every horizontal distance increment of 59 m (resolution of the DEM data set) was determined along a line within the flow path from source to deposit termination and the slope found by trigonometry and plotted as a continuum. Reported slope angles are tangents measured on the slope plots. Actual on-slope lengths of flow deposits are measured from slope plots, with the maximum apparent runout reported irrespective of subunits that terminate in less distance. Comparison of slopes in the highland and mare sites was made to investigate the possible influence(s) of differing target materials and granulometry.

2.2. Surface Area

Areas of the plan view of deposits were measured using an ArcMap outline tool. This underestimates actual on-slope area, which was approximated by multiplying the measured area by the factor of the actual runout distance divided by the horizontal distance (see section 2.1). This is an approximation, but in any case the outline generally encloses multiple deposit units so the area determined is only suitable for making order-scale comparisons. Each deposit was split into nine segments, and these were measured 3 times, with the average summed with that of other segments to give a best estimate.

2.3. Thickness and Volume

Deposit thickness and hence volume is problematic to measure. The aim was to derive thickness approximately from shadow lengths, using shadows 3 pixels or more in size and with known viewing geometry. As with the areas, nine deposit segments were created with three measures intended for each (i.e., 27 measurements for each deposit). However, some sections showed no clearly suitable shadows and some measures were obviously anomalous outliers (mainly from protruding large boulders), so these were excluded. Where possible (Table 2), the modal shadow length value was taken and then used to calculate the thickness (height) of the deposit segments, using trigonometry (see Table S1 giving image phase angles). Among the many limitations to the accuracy of this are the assumptions that the surface in shadow is flat and that the measured thickness is representative. This latter issue is nontrivial, as levees commonly are taller than channel contents, especially so where there has been material draining.

Segment on-slope areas and thicknesses were coupled to determine the segment volumes and these then summed to find a total. Due to the considerable limitations in finding representative thickness and actual slope areas, the volumes given in Table 2 can only be considered very approximate absolute maxima and quite uncertain. Further, some maxima manifestly are for deposits that include several to many tens of flow-deposit units, so that the volumes do not relate to discrete avalanches. Nevertheless the order-scale contrasts found are significant in relating to flow-deposit type.

3. Results

3.1. Study Sites Overview

Sites studied were chosen for their well preserved (little-degraded) and well-illuminated mass wastage features amenable to measurements (Table 2). LROC-NAC images have resolutions down to ~0.5 m/pixel, so abundant clearly visible boulders ($\geq$1.5 m or at least 3 $\times$ 3 pixels) are taken to indicate emplacement age younger than 300 Ma, and their occurrence is recorded for each site. We define mass wastage deposits with $>$20% of the flow unit bearing a content of boulders $>$1.5 m as being boulder-rich "coarse debris," and boulder-poor "fine debris" with a $>$1.5 m boulder content $<$20%. Typically, the boulder-rich deposits, or components of them, are darker in albedo, suggesting that grain size sorting may have occurred during flow. It is challenging, however, given the scale of the NAC images, to put any further constraint on the exact grain size range of the deposits.

The following sections include one case study showing a full diversity of phenomena in one area, and succeeding sections highlight some significant variations and/or reflect comparisons of mare and highlands crater target rocks. All but one of our site images are orientated with lunar north upward, the one exception being noted in its caption, and most images show the downslope direction with a dashed arrow. Supporting information Figure S6 gives the location of the studied craters on the Moon, and the context and topographic setting of each study site is shown in Figures S7–13.

3.2. Kepler Study Area

Kepler crater (latitude 8.13°N, longitude 37.98°W) is in mare basalt of Oceanus Procellarum and has a Copernican crater count absolute model formation age of ~1 Ga [*Hiesinger and Head*, 2006]. The study area, in the northeast segment of the crater (Figure 1), includes an extensive section of degraded fault scarp with associated deposits, at the northern end of the prominent subsided fault block bench. Subsidence style in the crater was asymmetric, by downsag with concentric faults and inward rotation in the west, forming inward dipping surfaces, and with normal faulting and bench formation in the east. Relatively smooth central areas comprise melt-rich units [*Öhman and Kring*, 2012].

Kepler shows diverse mass-wasting features, extending from high source cliffs of basalt layers, broken by numerous alcoves and gullies, down through vast slopes of flow-scarred granular deposits, to base-of-slope multiple overlapping aprons and fingered lobes with abundant coarse debris (Figures 1b and 1c). The manifest abundance of boulders $>$1.5 m implies their emplacement since 300 Ma, and paucity of impact marks in some relatively pristine deposits shows that mass wasting in Kepler has been persistent. From crater rim to (bench) floor here is ~2 km vertically. Beneath the cliffs, slopes are ~36° to 34.5°, the midslopes are ~33° to 32°, and these grade to lower slopes where mass wastage deposits are abundant at 29° to 24°. Locally "adverse" slopes, near horizontal and/or with rises of a few meters, occur at the foot of the main

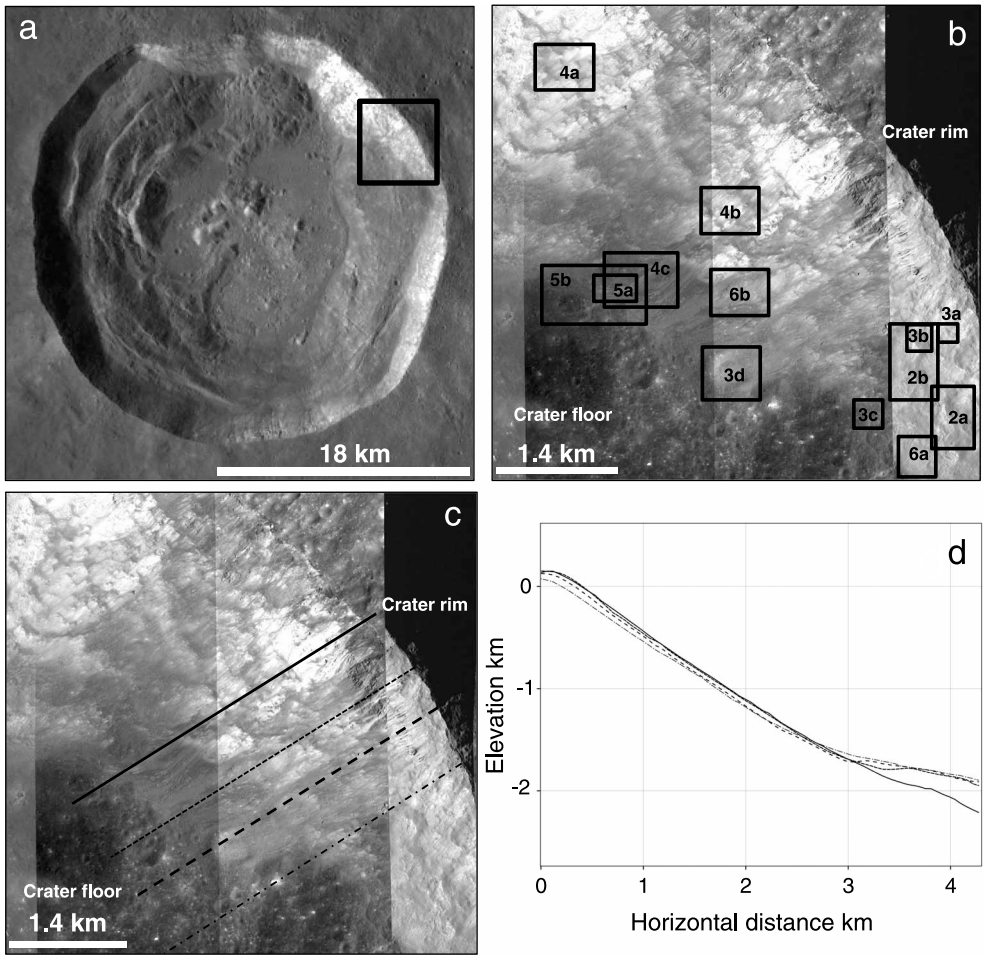

Figure 1. (a) Kepler crater and study area (box). The crater diameter is 31 km, with an average depth below the rim of ~2.7 km and with the highest parts of the northeastern (top right) rim crest rising ~3.2 km above the crater floor. (b) Study area showing locations of succeeding text figures that illustrate details. Near the crater rim are outcrops of basalt layers with intervening alcoves and gullies that lead down to slopes streaked by erosion and deposits due to mass wasting. (c) Study area showing location of profiles presented in Figure 1d. (d) Selected rim-to-floor topographic profiles in the study area. Elevation is relative to the lunar geoid. LROC-WAC Mosaic global 100 m image and LROC-NAC image frames M186134194RE, M173165404RE, M133078533LE, and M1129731152LE courtesy of NASA/GSFC/ASU.

escarpment, although slopes mostly continue across the broad bench with inclinations between 22° and 9° (Figures 1c and 1d). Debris tracks from source to termination mostly extend downslope ~ 2.5 km, rarely up to ~3.5 km.

3.2.1. Ledges and Debris Fall Deposits (Talus)

The crater wall is variably covered by mass wastage debris, less so in the upper few hundreds of meters where discrete basalt layers are exposed. Deposit grain size variations are evident in patterns of relatively dark and relatively pale albedo, traversed by slope-parallel streaks (Figure 1b). The darker patches, which tend to darken downward to irregular, broadly transverse but discontinuous edges, are interpreted as recording former topographic ledges that are now almost entirely buried by coarse talus. The intervening areas of paler albedo lack such talus and the slope-parallel streaks that cross both dark and pale areas with little or no deflection evidently mark erosion and/or deposition by debris that streamed downslope to accumulate mainly at the slope base in overlapping aprons and lobes (see also section 3.2.2). The limited deflection of the streaks, and the slope-parallel topographic profiles (Figures 1b and 1d), indicate that the talus-buried ledges now have little or no topographic expression. The overall pattern is interpreted as recording early collapse-subsidence of slivers of strata that detached on faults in adjustment of the initially over steep walls that had formed behind the main fault block (bench). Loose falling debris then accumulated on the early

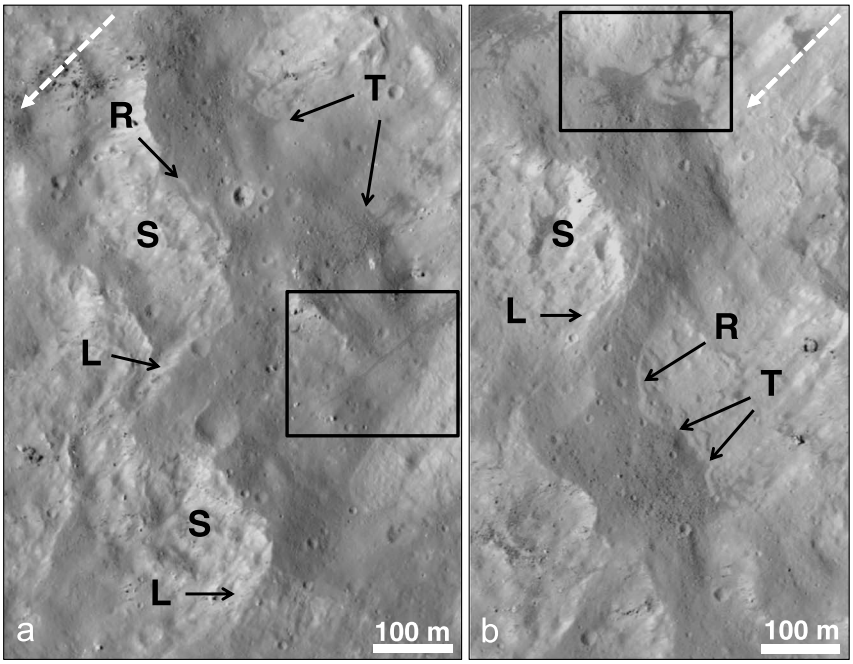

Figure 2. (a and b) Examples of crater wall ledges. Ledges with relatively thick deposits are separated by normal-fault scarps with thinner or little cover (streaked pale). Many scarps (S) curve into and are linked by lateral detachments (L). Both scarps and ledges have superimposed small (<20 m) impact craters, although those on the steeper slopes are less well formed. Talus cones and aprons (T) have formed at the back of ledges against scarp slopes, primarily from incremental debris fall, as in screes on Earth. Debris flow leveed finger deposits cross talus cones (located in boxes, and see Figure 3b for detail), recording relatively sustained mass flux and continuity of inward slopes across ledges. Streaks on fault surfaces record local deposition and erosion by passage of debris. Coarse debris here is relatively scarce. In a few places, short steps following adjacent scarps (R) possibly record slight fault reactivation and/or slope deformation (see section 3.2.3). LROC-NAC image frame M133078533LE courtesy of NASA/GSFC/ASU.

formed ledges to build talus to its angle of repose. This constituted catastrophic mass wasting consequent on initial formation of Kepler and was the main process that rendered the slopes at a large scale nearer to stable repose.

Slope-parallel streaks are less abundant in the southeast of the study area (Figure 1b), where the ledges buried by debris fall deposits and intervening original fault plane slopes appear less reworked (Figures 2 and 3) and have relatively little coarse debris exposed at the surface. Here the ledge-covering deposits slope continuously down toward the more thinly covered, paler slopes beneath (Figure 2), and it is widely evident that deposits thicken to the back wall in apron-like wedges and cones or fans with apices within and beneath gullies (Figures 2 and 3). Some well-defined aprons and fans clearly grade finer grained upward (Figure 3). This is characteristic of momentum-governed debris fall in which more massive material bounces and rolls farther, as with terrestrial screes. In a few instances leveed debris flow deposits extend down across the debris cones and fans, highlighting both the slope continuity and the contrast of emplacement styles (Figure 2).

One small impact crater, ~500 m in diameter and located at the base of the main-wall slope (Figure 3d), shows well the entrapment of runout debris fall boulders. These are concentrated on and near the base of the opposed slope, and their capture has caused a runout "shadow," or paucity of this material, farther away (to left; compare with top left); the largest boulders mostly traveled farthest, some making it up onto the opposed wall and rim. This crater also trapped a bouncing boulder that crossed its wall obliquely before final roulette-ball-like capture (1-1-1-1-1; note the final downslope trace and culprit). Bounce marks at 2-2 are proximal parts of a 2.1 km trail formed across the bench by a ~15–18 m boulder.

3.2.2. Debris Flow Deposits

The steep crater wall, grading down from 36° to 34.5° to 32°, is widely marked by countless slope-parallel streaks that record both erosion and deposition by debris flows. These features mainly originate amidst the outcrops and alcoves or gullies where the bedrock basalt is exposed for several hundreds of meters

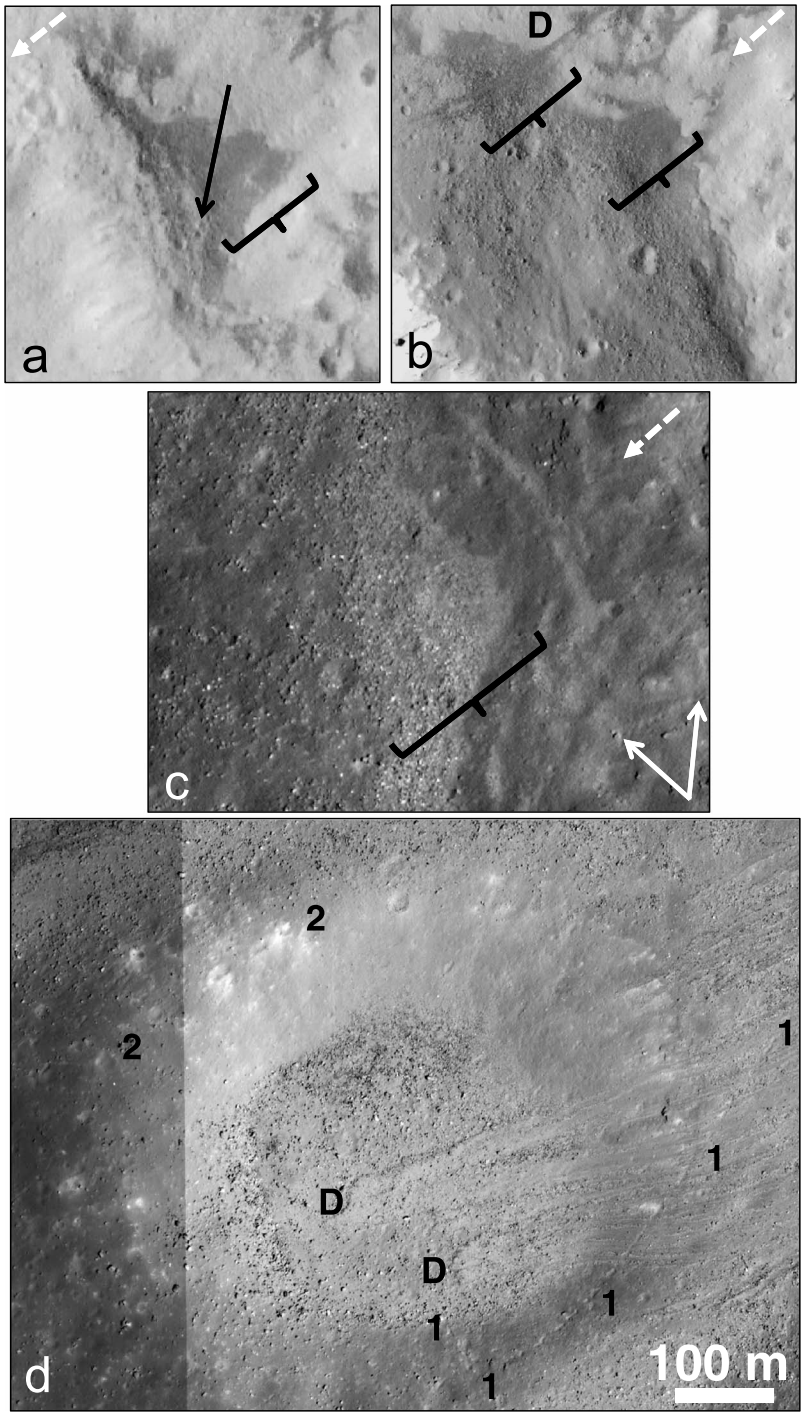

Figure 3. (a–c) Slope break graded debris fall talus cones (bracketed) formed on ledges on top of fault slivers (all fields of view ~200 m wide); cone apices are upslope (toward top right), with coarse debris near the cone base and momentum runout boulders beyond. Pale streaked surfaces are degraded fault scarps with variable cover of regolith, locally cratered. Debris flow deposits (D in Figure 3b) emanate from a gully and cross a talus cone. Steeper slopes show downslope striations, some of which clearly are boulder bounce trails (arrows). (d) Degraded crater at the base of the main wall (above top right) shows asymmetric distribution of momentum runout debris fall boulders, concentrated on the opposed, left-hand slope, reflecting capture of material that otherwise would have traveled farther, as in the top of the image. The general surrounding slope here is ~9°, and the crater is a few tens of meters deep. Debris flow deposits (D) showing coarse-grained levees and lobate terminations with impounded (pale) finer debris extend onto the crater floor, partly burying boulders there. Trails from bouncing large boulders (e.g., 1 and 2) are also evident (see text). LROC-NAC images M173165404RE, M133078533LE, and M1129731152LE courtesy of NASA/GSFC/ASU.

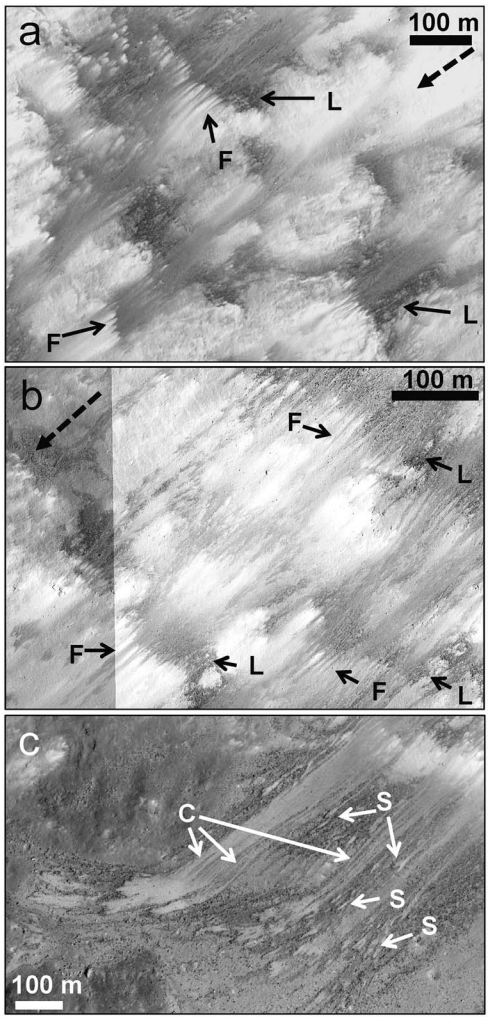

Figure 4. (a and b) Debris flow deposits extend more or less continuously down across ledges strewn with darker, relatively coarse debris, mainly talus, which has in places been remobilized to form downward tapering fingers that extend from the ledge edges. The slopes here are 33° to 32°, and the paler diffuse streaks are taken to be deposits of relatively fine debris that was mobilized nearer to the crater rim. The tapering of the dark fingers suggests redeposition of some coarse debris that moved as bed load in debris flows below the ledges. (c) Lobed and fingered flow-deposit terminations occur at the slope base beneath the diffuse streaked pale deposits and sharply tapered coarse fingers (top right and Figure 4b). The slope with these deposit terminations generally diminishes from 32° to ~24°, locally slightly less for the more extensive deposits. The flow deposits show pronounced granular segregation; coarse dark levees confine channels and terminal deposit margins, and on the lower slopes pale finer-grained fractions (fines) are ponded behind these. Some starved flows terminated on the steeper slope (e.g., labeled S) where fines also are impounded by coarse levees. On the steeper slopes in this view, many coarse (darker) levees bound partly drained channels (C) lined with fines. The fines have partially drained to the deposit front and ponded there behind terminal levees. Downslope beyond the leveed deposits, impact craters and bounce-roll trails (low right and low left "foreground") in the regolith are relatively abundant, showing that the uppermost leveed deposits are relatively young. This sediment wedge is widely close to repose and hugely multiple in origin, comprising innumerable overlapping flow units. The upper part of this slope, at 32°, is taken to reflect the dynamic angle of repose for the coarse debris. LROC-NAC image M173165404RE courtesy of NASA/GSFC/ASU.

below the crater rim (Figure 1b), and they commonly terminate near or at the base of the steep wall, at 29° to 24°, with dark, coarse-grained levees that impound pale-colored finer material. In midwall areas, at 33° to 32°, diffuse midgray streaks cross ledges occupied by darker, coarse material taken to be ancient talus, and this evidently has been remobilized (eroded) and partly redeposited to form downward tapering fingers extending from the ledge edges (Figures 4a and 4b). The distinctive dark fringes beneath the ledge edges are here called "sharply tapered coarse fingers." The midgray diffuse flow deposits apparently remain from coarse-fine (polydisperse) granular mixtures that segregated during flow and, toward flow terminations, formed coarse levees that channeled and then enclosed the finer debris (Figure 4c).

Laboratory experiments (Figure S4) confirm that coarse deposits that rest stably at their angle of repose, like the talus on ledges here, can be mobilized by infiltration of finer material (typically sand grade) that has a lower repose angle and flows across them. In section 4 we consider gravity and the scaling from our experiments and confirm the probable equivalence of the lunar remobilization processes.

Kumar et al. [2013] show similar, but not identical, lunar features, which they ascribe to debris flow and refer to as "dark slope streaks." As in Kepler crater, many of those streaks extend as fringes off the edges of ledges where the dark deposits accumulated and predate pale-colored fine debris that extends onto them. However, those dark streaks do not taper into diffuse pale deposits. Apparently the Kepler slopes were sufficiently steep and near the repose angle of the finer debris so that fines-rich debris flows swept down much of the wall to the crater floor and in doing so substantially mobilized the coarse material as it became inundated on the ledges. The impact record in the Kepler

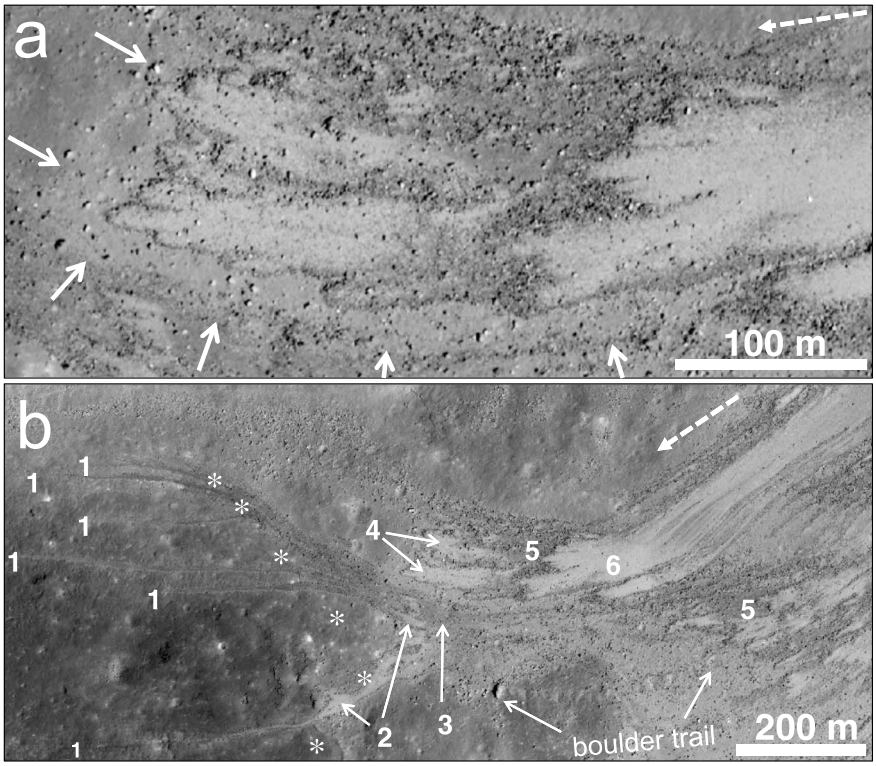

Figure 5. Debris flow deposit terminations. (a) Lobate coarse-leveed terminations at the slope base "impound" finer deposits (pale) and show a multiple-event succession, with successive flows showing shorter runout. Dark material lacking clear margins here is spread and separates the two main lobed deposits. "Nearer" along the slope (see Figure 4c) this darker material has weak/small levees and lobate terminations, which suggest that it contains and segregated some relatively coarser sediment. Diffuse veils (arrows) of relatively fine debris widely trace around steep leveed margins. (b) Early debris flow(s) evidently were deflected and caused to deposit at a low topographic barrier (position approximately marked by asterisk line and shown in Figures 1c and 1d), beyond which relatively narrow coarse-leveed fingers, labeled 1, continued to form for hundreds of meters. Pale finer debris, labeled 2, indicates that succeeding flow(s) were channeled between earlier levees but mostly unable to surmount the barrier. Midgray boulder-rich deposits, labeled 3, lap onto 2 and are overlain by pale fringing veil deposits that surround the lobate margins of 4 (see Figure 5a). Similar pale deposits occur widely in front of the lobate units to the southeast (lower right). These, in turn, are overlain by coarser deposits with poorly defined margins, 5, while coarse-leveed lobate terminations with impounded fines, labeled 6, appear to be the youngest debris flow deposits here. Also shown is the trail of a boulder, with long axis diameter 20–25 m, which evidently bounced somewhat before stopping. Other large debris fall runout boulders, of several meters scale, locally overtopped the barriers to rest on the far side. LROC-NAC image M173165404RE courtesy of NASA/GSFC/ASU.

heavily streaked slope is substantially obliterated (compare with an area to southeast, e.g., Figure 2), consistent with the paucity of impact indications in the base-of-slope correlative deposits, which clearly are among the youngest here (Figure 4c). The general paucity of impact craters on this slope area suggests ongoing triggering and avalanche activity.

Pale veils of relatively fine deposits clearly surround the periphery of some leveed terminations (arrowed in Figure 5a) and are extensive in front of such units elsewhere (Figure 5b). They appear to thin, becoming less distinct, with distance farther from the lobed fronts. From this spatial association, the veils appear genetically related to the levee-forming granular debris flows. We interpret the veils as due to draining of fines through the adjacent coarse levees that impound such material. This phenomenon is apparent at other crater sites of similar flow unit terminations, and we defer a fuller account of it to the discussion (section 5).

Beyond the youngest flow deposits at the slope base there are adverse topographic barriers locally surmounted by elongate coarse-leveed fingers of earlier formed debris flow deposits (Figure 5b). Evidently, these earlier flows were relatively mobile, with greatest runout, and, although impeded and thus caused to deflect and deposit in part at the barriers, some flowing material continued over them to form narrow

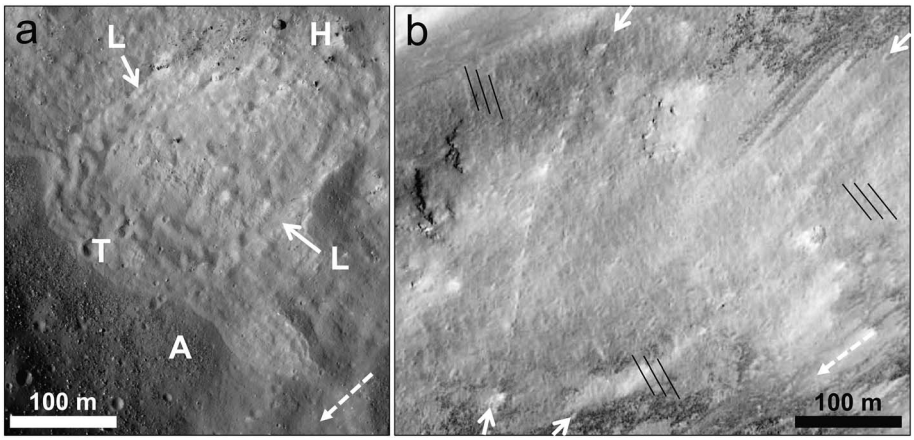

Figure 6. (a) Small degraded slump, showing concentric headwall extensional detachments (H), low-end (toe) sinuous compressional ridges (T), and linear lateral detachments (L). The slump surface is scored with abundant impact marks and debris fall boulder trails, and the toe is partly buried by a graded talus apron (A). A ridge that follows the slope base to the northwest of the slump may relate to general creep above. (b) Creep patterned slope at ~32°. Irregular low-amplitude (indistinct) corrugations are transverse to the slope, parallel to the drawn triple sets of lines. The slope is crossed by several boulder bounce trails, the more prominent of which (arrowed) are oblique to slope (left) and downslope (right). LROC-NAC images M133078533LE and M1129731152LE courtesy of NASA/GSFC/ASU.

fingers extending several hundreds of meters on slopes of ~27° to 22°. Successive debris flows apparently were less mobile, with lesser runouts. Boulder-rich deposits with poorly defined margins (labeled 3 and 5 in Figure 5b) record relatively widespread flow, apparently less confined by formation of levees. Conceivably, the early debris flow runout was greater because the original avalanche volumes were relatively large and the flows were, thus, more sustained, and/or the flows on the slopes above were more strongly channelized, with sustained flow from a narrow, efficient "conduit" that restricted spreading. It is not likely that the earlier (but long-degraded) crater wall slope was any steeper. However, it is possible that the more mobile debris flows, including the boulder-rich spreading varieties, originated from collapse of mixed (polydisperse) material from the cliff source(s) high above, whereas the later, strongly leveed flows resulted (as inferred above) from slope failures and flows of fines that remobilized coarse debris from lower ledges. These latter debris flows, resulting from repose slope failures, may thus have had less potential energy than collapses among the high cliffs.

3.2.3. Slumps and Creeps

A degraded slump is preserved at the base of slope in the southeast of the study area (Figure 6a). It has classic horseshoe shape, ~200 m wide across slope and >300 m long, with headwall extensional detachments, toe compressional ridges, and lateral detachments. It bears the scars of many small impacts and trails of overpassing debris falls, and its downslope termination appears to be partly buried by an undeformed graded talus apron. From these features, the slump is presumed to have formed relatively early in the Kepler slope development.

Slopes dominantly of debris with pale albedo and showing abundant impact craters at tens of meters scale, as well as boulder bounce-roll trails, widely show creep features (Figure 6b). These are transverse-to-slope, discontinuous and slightly undulose, low-amplitude corrugations with spacing typically at 5–20 m. They resemble terrestrial solifluction creep features that typically result from freeze-thaw but here relate to impacts and ground shaking [see also *Xiao et al*., 2013]. Crater-forming disturbances show only limited downslope movement of displaced material, of tens of meters with the deposit tapering downslope, indicating that the creep affected a general slope less than the local angle of repose. Here the slope is measured at ~32°, whereas it is steeper, ≤34.5°, where boulder-poor debris was readily mobilized to form flows that crossed talus-strewn ledges. Ridges at the lower ends of extensive corrugated slopes may reflect slope foot creep-related folding, akin to slump toe deformation but lacking discrete headwall and lateral dislocations (Figure 6a).

3.2.4. Boulder Trails

Kepler crater midwall slopes and base-of-slope areas are patterned by numerous bounce and roll traces of large boulders (tens of meters in diameter), especially plain to see in pale-colored boulder-poor material.

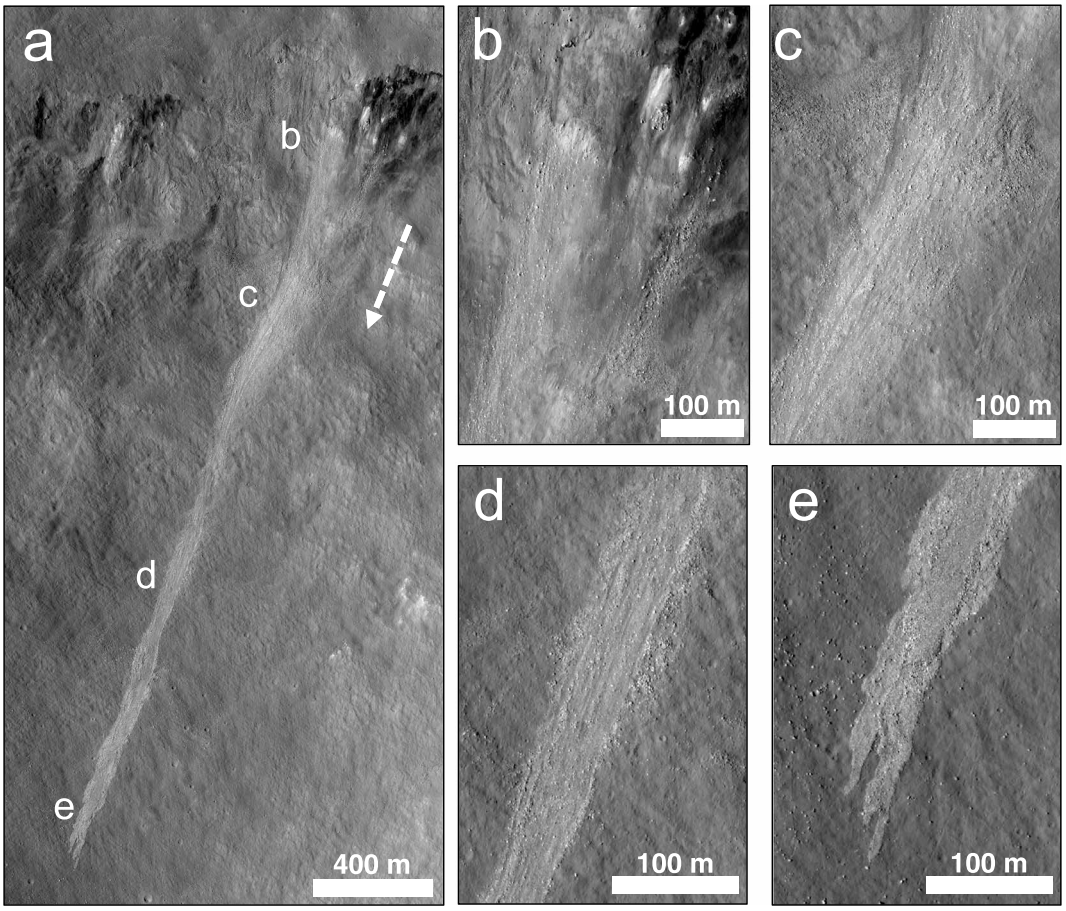

Figure 7. Gambart B debris flow deposits. (a) Full 2.9 km runout from source cliffs to distal termination showing locations of Figures 7b to 7e. (b) Source rock exposures (pale) above proximal slope at ~33.5° with scattered boulders and numerous diffuse streaks recording both erosion and limited deposition by mainly overpassing flows. (c) Upper medial reach at ~32° with scattered boulders and numerous slightly irregular and locally crossing boulder-free channels (darker traces). (d) Lower medial reach at 29° with pronounced marginal and internal coarse levees bounding distinct channels containing finer debris with some isolated boulders. (e) Distal deposits at 27° comprising stacked flow units with boulder-rich lobe and finger margins and upslope partly drained axial channel (see Figure 8). LROC-NAC image M135263529RE courtesy of NASA/GSFC/ASU.

The boulders commonly originate high on the crater wall, and some traces trend significantly oblique to the slope (e.g., Figures 3d and 6b). The oblique trails could have formed from material dislodged by an impact on the upper wall or could have been injected as distal ballistic ejecta from large cratering events in the vicinity of Kepler; in either case the culprit boulders do not simply represent material directly upslope above their resting place. The longest bounce-then-roll boulder trail in the study area is ~2.1 km, extending across low slopes and originating at an initial impact site near the base of the main crater wall (trail labeled 2 in Figure 3d). Given its low starting point, its momentum may not have been derived from height (potential energy) on Kepler wall.

3.3. Gambart B Debris Flow Deposits

Debris flow deposits are prominent on the north side of Gambart B impact crater (latitude 2.15°N, longitude 11.35°W), which was formed during the Eratosthenian period (3.2–1.1 Ga) [*Hawke et al.*, 1991] in basalts of Mare Insularum. The crater has a simple bowl morphology, ~11 km in diameter and up to ~2.4 km deep. The deposits have limited lateral extent (Figure 7), extending from a cluster of prominent cliffs below the rim for ~2.9 km down a gently shallowing slope, from ~34° near the top (locally 38°) through 32° to 29° on middle to lower slopes and ~27° at the distal end. Abundant boulders $>$1.5 m register emplacement since 300 Ma.

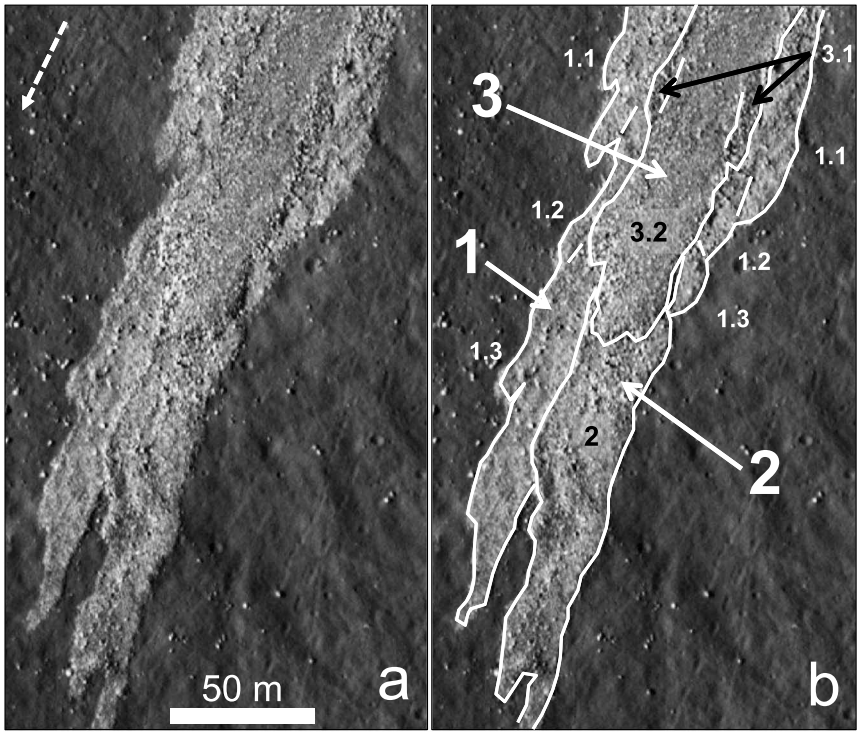

Figure 8. Termination of the Gambart B flow deposits. (a) Base image. (b) Interpretations of deposit units and subunits. Superposition of flow units 1 to 3 is clear, with 2 having slightly longer runout than 1, and 3 the least runout. Units 1 and 3 apparently formed with pulsed advance recorded by successive breakthrough of rounded (lobes and small fingers) margins, 1.1–1.3 and 3.1–3.2. Subunit 3.2 shows a terminal mound with upslope partly drained channel within 3.1. Such a tentative scheme is difficult to apply in places, so subunits remain uncertain in detailed correlation. LROC-NAC image M135263529RE courtesy of NASA/GSFC/ASU.

The deposits record numerous flow paths. Abundant slightly irregular and locally crossing, weakly defined channels merge downslope to form fewer and straighter channels that have relatively pronounced coarse levees and intervening finer debris that locally surrounds some boulders that are relics of former levees or deposited original bed load. In the lowermost ~0.7 km (Figures 7d–7e) deposits are more substantial along the margins of a main channel way, and in the final ~0.3 km, where the slope is ~27°, a strong tendency to deposit is evident where the front advanced in spreading mass surges, with succeeding surges breaking through and reaching farther (Figure 8). An elongate finger records the maximum runout, with a final and lesser surge forming a relatively short overlapping finger with a partly drained channel behind.

The multiple flow paths in medial and upper reaches beneath a moderately broad source terrain indicate multiple flows. It seems impossible, however, to tell whether these were formed from a wide and more or less simultaneous collapse at source that constituted a single highly unsteady event or whether there were numerous smaller individual collapses spread through time or both extensive and limited collapses. Whatever the case, the flows and/or flow surges were increasingly channelized toward lower slopes where they sequentially formed overlapping lobes and fingers. While the successive flows and/or surges are likely to have reworked previous deposits, there is no evidence here that preexisting slope deposits at repose were remobilized, as seen at Kepler (Figure 5b).

3.4. Bessel Debris Flow Deposits

A succession of various mass wastage deposits occurs in the southeast sector of Bessel crater (Figure 9), in Mare Serenitatis (latitude 21.8°N, longitude 17.9°E). The crater is isolated, circular to slightly polyhedral in morphology, and ~16 km in diameter with a maximum depth of ~1.8 km. It formed during the Copernican period (<1.1 Ga) [*Campbell et al.*, 1992] in basalt lavas of 3.5 Ga age [*Hiesinger et al.*, 2000; *Hiesinger and Head*, 2006]. The crater has a superimposed bright impact ejecta ray, the origin of which is debated to be

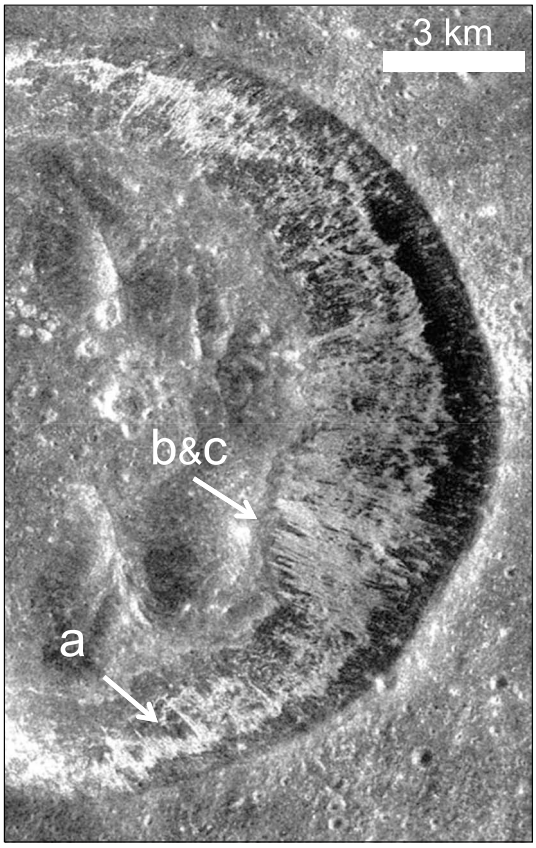

Figure 9. Bessel crater showing a portion of LRO Mini-RF instrument radar image (~30 m/pixel spatial resolution, image name LSR_CDR_LV00). Labels locate panels shown as close ups in LROC-NAC images in Figure 10. Image courtesy of NASA/GSFC/JHAPL.

Menelaus or Tycho to the SW [*Campbell et al.*, 1992]. Abundant boulders >1.5 m imply deposit emplacement since 300 Ma.

Crater wall cliff exposures of basalt lava are widely continuous just beneath the crater rim. The in situ lava flow units are strongly fractured (Figure 10a), with alcoves and gullies within and at the foot of which are apices of talus cones and aprons, seemingly mostly of relatively fine debris (labeled 4 in Figure 10a) with coarser material below (labeled 3 and 2 in Figure 10a). The darker exposures labeled 3 in Figure 10a are inferred to be where erosion due to passing debris and/or retrogressive slope failure has uncovered coarser material. The pale deposits labeled 2 in Figure 10a locally grade laterally into coarse talus, and these variable deposits extend downward onto, and partly obscure, coarse-boulder-bearing deposits that in places extend farther as distinctive lobes and fingers (labeled 1 in Figure 10a). Similar relations occur with pronounced fingering deposits farther northeast (Figures 10b and 10c), where the long fingers proximally are partly buried by finer material. Thus, these lobes and fingers are considered to be relatively early debris flow deposits, with their proximal reaches buried by later development of fans and aprons dominantly created by debris fall.

The distinctive long, boulder-rich fingers in places extend up to ~2 km downslope from the foot of the basalt escarpment, in middle reaches at 32.5° to terminations at 31.5°. In marked contrast to Gambart B deposits (Figures 7 and 8), each finger is longitudinally quite uniform, lacks a drained channel, and appears similar in width and height to the others. Close proximity and parallelism with neighboring fingers, with local contact, is characteristic. Strikingly similar multiple fingers are also produced in laboratory experiments [*Woodhouse et al.*, 2012] when a single polydisperse granular mixture is released from a linear-source hopper and segregates during flow down a near-repose-angled slope (Figure S5). The fingers initiate as fairly regularly spaced flow front instabilities that form lobes and then, if the mixture contains a sufficient concentration of coarse particles, fingers grow from these. The finger pattern at Bessel is, thus, interpreted as recording simultaneous debris flow finger advance from large-volume collapses involving abundant coarse material from long sections of the basalt cliffs. One or more large-energy triggering event is implied. The succeeding fans and aprons formed gradually, mainly by debris fall, after the main event(s). The Bessel flow-deposit volume of ~15.2×10^6 m^3 (Table 2) relates to the prominently fingered unit labeled b and c in Figures 9 and 10 and is by far the most substantial deposit studied, irrespective of uncertainties in volume estimations (section 2.3).

3.5. Censorinus Crater Debris Flow Deposits

"Large-event" deposits (Figure 11) are striking in Censorinus crater at the edge of Mare Tranquillitatis (latitude 0.47°S, longitude 32.73°E). The crater is 3.8 km in diameter, ~1.1 km deep, and apparently young, with a nighttime temperature anomaly indicating abundant basalt boulders [*Moore et al.*, 1980]. Avalanches originate at and close to the sharp crater rim, and runout reaches ~2.1 km. The main crater slopes, at 32.5° to 32°, display myriad tracks that reflect both erosion and some deposition, i.e., mainly overpassing of debris (Figure 11a). These lead to the slope base where there is a relatively abrupt slope change beyond which are two distinct sets of short-fingered lobe deposit accumulations at ~25°. The deposits have the form of cat's paws, the later

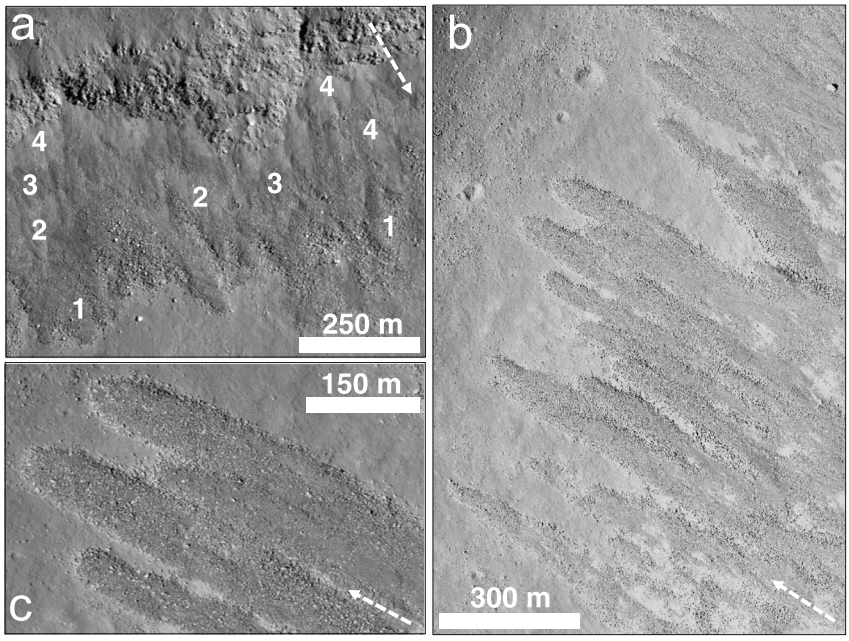

Figure 10. Bessel crater wall debris flow deposits. (a) Inverted image (south is up) of southern crater wall basalt cliffs and successively younger, superimposed deposits that build a depositional wedge sloped at ~32° against the wall. Early debris flow deposits (1) are coarse-grained fingers partially draped and obscured by a variable apron (2 and 3) of merged debris fall cones with finer-grained apices (4) within and below rock alcoves. (b) Coarse-grained debris flow deposit fingers extending at ~31.5° from the southeast wall foot (out of sight but similar to the wall in Figure 10a). The fingers are partially mantled by boulder-poor deposits that increasingly cover the finger tops toward the cliff but otherwise appear to have infiltrated into the coarser marginal deposits beneath. The coarse-grained fingers appear fairly uniform in grain size composition, width, and thickness along the slope beneath the cliff, and they show little or no channel draining. (c) Enlargement of Figure 10b. LROC-NAC image M135073175RE courtesy of NASA/GSFC/ASU.

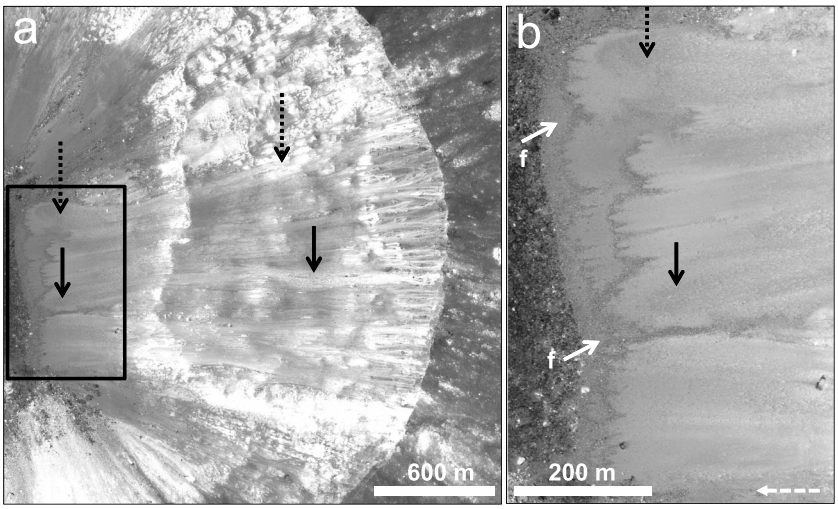

Figure 11. Censorinus crater debris flow deposits. (a) Rim-to-floor extent of flow deposits on the east side of the crater. Black arrows indicate two of the main upper traces of erosion and diffuse deposits leading down to lobate deposits with "cat's paw" morphology at the slope base. These traces slope from 34° near the top to a consistent 32.5° to 32° for 1.5 km before the terminal accumulation with an abrupt slope change to ~25°. The lateral limits of the deposits are mostly not sharply defined, and the thickest deposits are at the slope base (box). (b) Detail of the base of slope (box in Figure 11a) showing an earlier and a later (overlying) set of cat's paw lobes, lacking any features of draining and recording two large (main) debris flow events. A fringe of pale deposits (labeled f) extends for tens of meters beyond the coarse front of the lower set of debris flow deposits. LROC-NAC image M139694087RE courtesy of NASA/GSFC/ASU.

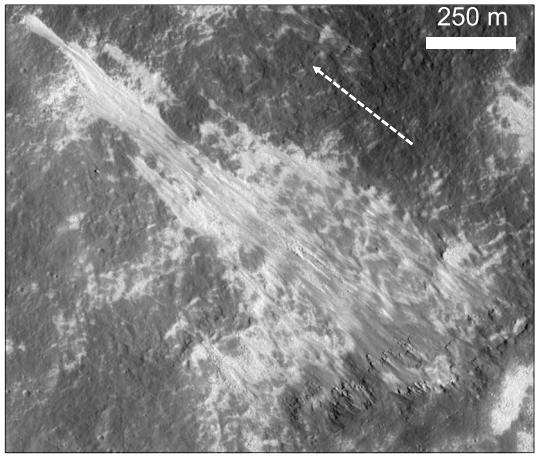

Figure 12. Riccioli CA crater multiple debris flow deposits originating from small cliffs formed of feldspathic basin ejecta and emplaced on highlands surficial regolith. The maximum runout is ~1.75 km down a slope smoothly graded from ~34.5° to ~27°. Irregular pale patches are boulder-strewn zones that in many places have been swept by debris flows with the coarse debris transported farther and redeposited in levees, especially on the lower slopes. LROC-NAC image M112074670RE courtesy of NASA/GSFC/ASU.

emplaced (upper) set not extending as far as its predecessor (Figure 11b). Each set is taken to record simultaneous avalanching of substantial amounts of debris from an elongate segment of the crater rim, in a single large event. The upper surfaces of the fingered-lobe deposits are extensively overlain by boulder-poor deposits, and the entire slope above is streaked with boulder-poor material. Conceivably, the finer debris lagged behind the boulder-rich catastrophic avalanches and were derived from them, but it also seems likely that the slope could have shed material frequently in response to any shaking.

The cat's paw lobe-and-cleft deposits are closely akin to the early, partly buried deposits described from Bessel crater (Figure 10). The form is characteristic of simultaneous and sustained advance on a broad front (Figure S5), so that extensive and voluminous collapses from a broad source are inferred. In contrast, piecemeal small collapses would tend to produce irregular overlapping piles of small-volume deposits, as at the base of the main slope at Kepler crater (see Figure 5b). From the estimations of deposit volume (4–5 $\times$ 10^6 m^3; Table 2), we infer that the Censorinus collapses involved roughly 2.5–3 $\times$ 10^6 m^3 of dense rock simultaneously from extensive linear sources.

The Censorinus debris flow deposits show a pale fringing veil in front of the lower set of coarse lobate deposits (labeled f in Figure 11b). As for the similar veils at Kepler (Figure 5), this is interpreted as probably due to the draining of relatively fine sediment through the adjacent coarse-grained flow unit margins, although in this case such material may have flowed over the lobes and infiltrated the coarse-grained margins, which remain clearly visible. This is discussed further in section 5.

3.6. Riccioli CA Debris Flow Deposits

Numerous flow deposits are evident on the southeast wall of Riccioli CA crater (latitude 0.58°N, longitude 73.01°W; Figure 12). The crater is simple, 14.2 km in diameter, up to ~3 km deep and is Copernican aged (<1.1 Ga). It is situated on the northeastern distal ejecta blanket of the Orientale basin, on the edge of the Procellarum KREEP Terrane, but is considered "highlands" as it is in the outer Feldspathic Highlands Terrane [*Jolliff et al.*, 2000]. The boulder-rich nature of the flow deposits supports a flow age of <300 Ma. The slope deposits range down from ~34.5° to ~27°, from clusters of rock exposures below the crater rim through successive zones of numerous erosional and depositional streaks to series of coarse-leveed channels and a most distal mounded lobe, partially surmounted by fines. Evidently, some flows bulked up temporarily, where they swept through boulder fields and deposited the material in levees lower down.

3.7. Virtanen F Crater Debris Flow Deposits

Debris flow deposits unlike any yet described occur in the northeast sector of Virtanen F crater (latitude 15.76°N, longitude 177.31°E), within the far side lunar highlands megaregolith (Figure 13). The crater is simple and circular, ~11.8 km in diameter and with a maximum depth of ~3.5 km; the western part is dominated by impact melt seemingly originating from Virtanen crater, while the eastern half is where the subject deposits lie. The formation age is unknown, but presence of boulders >1.5 m in the substrate of the studied deposits suggests their age is <300 Ma; elsewhere creep-textured regolith is widespread.

From source to termination the maximum runout here is ~4.5 km, down a slope somewhat lumpy irregular in upper reaches to relatively smooth below and evenly graded down from 34.5° to 27.5°. On the

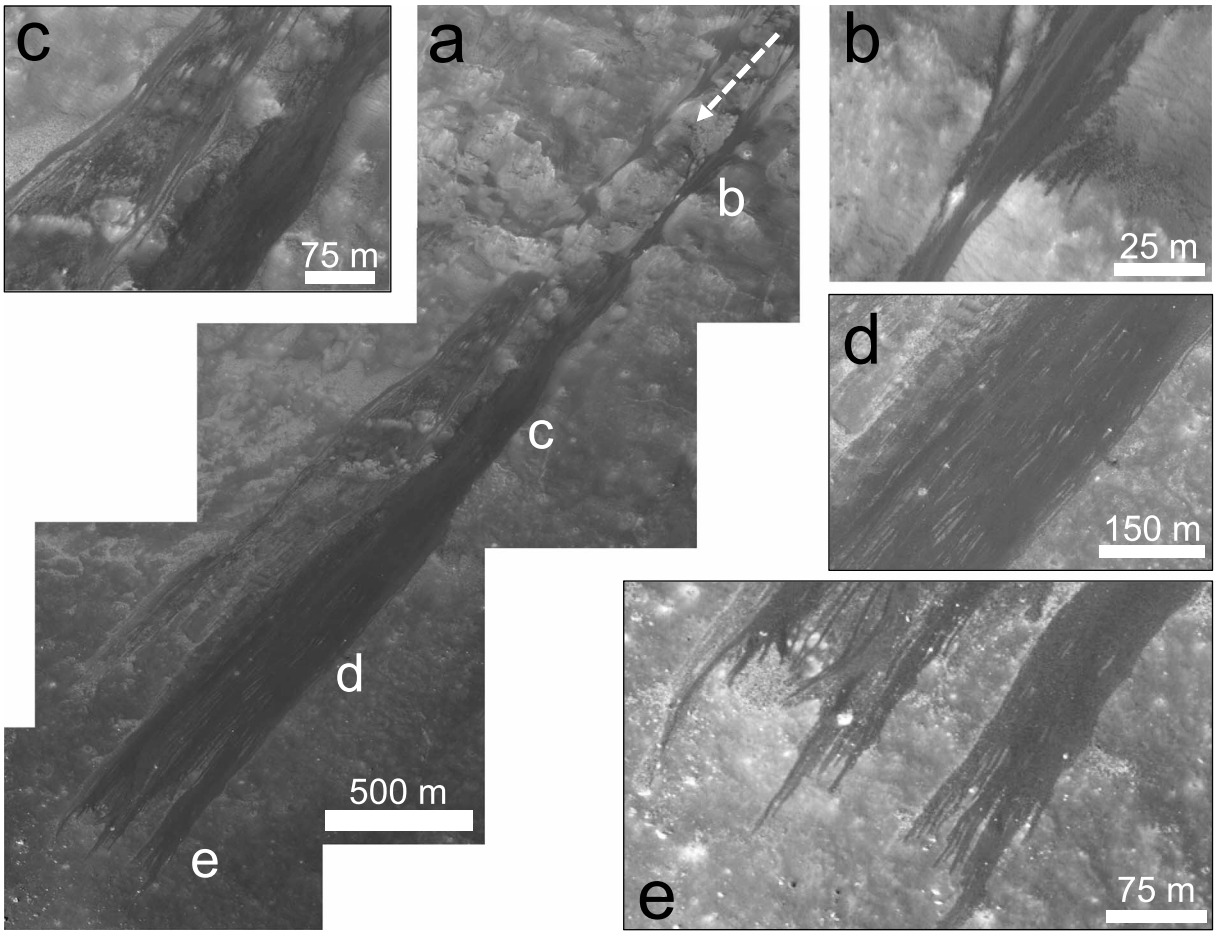

Figure 13. Virtanen F crater debris flow deposits with overall runout of ~4.5 km. The deposits are distinct for their darker color than the underlying substrate and manifestly multiple nature in lower reaches, where there are several tens of remarkably continuous narrow fingers. (a) Entire runout from just beneath the source(s) (see Figure 14b), showing locations of Figures 13b–13e. (b) Deposit trails are locally confluent according to topographic constriction, here traversing creep-textured regolith at ~33.5° above and below a narrow "ledge." (c) Flow paths diverge on slightly lesser slopes (~32°), locally originating from streaked pale slopes presumed to be dominantly sites of material overpassing. (d) Tens of narrow, ribbon-like fingers become distinct where the slope, at ~29.5 to 28.5°, is less irregular. The ribbon-like flow units are mostly subparallel, although in places apparently convergent and also divergent. (e) Flow unit terminations at ~27.5° are abruptly rounded or tapered and appear in bundles, in one instance (above prominent boulder) cutting across previous deposits; there are no (distinct) levees or terminal mounded accumulations. LROC-NAC image M169398317LE courtesy of NASA/GSFC/ASU.

slightly lesser midslopes downward the constituent deposits of this feature tend to diverge and then run subparallel. In many instances of apparent bifurcation it is not clear whether a single flow split into two or whether a following flow escaped from a predecessor path. In any case, lower reaches record several tens of remarkable, persistently narrow, ribbon-like fingers commonly only ~3–5 m wide. Unlike deposits previously described, e.g., Kepler (Figure 4c) and Gambart B (Figure 7), there are no obvious marginal levees bounding distinct channels and no pulsed and/or bulbous flow unit terminations. Rather, the terminations, which are on a slope of ~27.5°, are abruptly rounded or tapered. It appears (Figure 14a) that preexisting large boulders are embedded in slight, narrow, elliptical topographic rises in the host slope and that these rises (not the boulders) have deflected flows, causing deposit divergence upstream of the boulders and return convergence downstream. Smaller boulders show in some flow paths indicating that the deposits are thin.

The sources of the flows appear to be in alcoves that have scalloped headwalls (Figure 14b). These cut creep-textured regolith as well as bench-featured rock and they record retrogressive (upward propagating) failures that are unlikely to have released debris all at once. Rather, it seems that the mass wastage here was incremental through time, consistent with the many tens of deposit fingers below. The duration and trigger(s) of the mass wasting are unknown, but whether nearly continuous and highly unsteady, or discontinuous

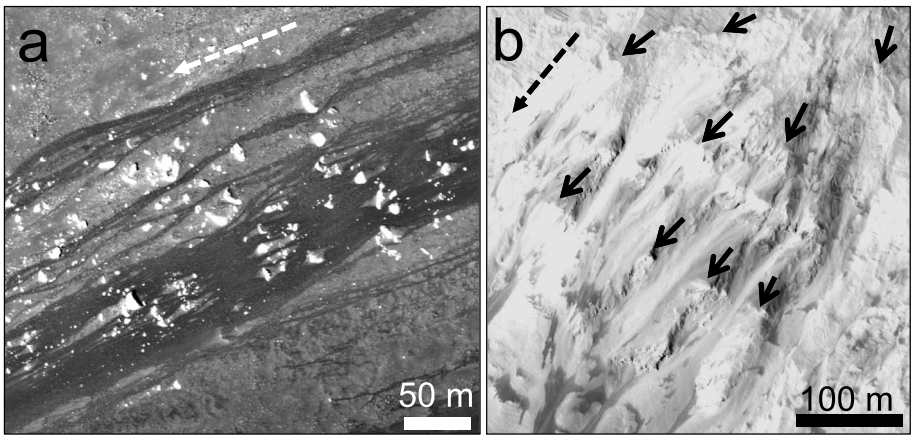

Figure 14. Virtanen F crater ribbon deposits and source(s). (a) Image of middle lower slopes at ~29° displaying numerous elongate, mainly parallel-sided, ribbon-like flow deposits, commonly only ~3–4 m wide. Large preexisting boulders are embedded in slight topographic rises such that flow paths diverge in deflections upstream of the boulder and converge downstream. (b) Source cliffs showing numerous headwall scarps, some (only) indicated with arrows, with intervening gullies. Uppermost slopes are creep-ribbed regolith, whereas discontinuous benches beneath appear to be bedrock. Scarp edges are scalloped and characteristic of piecemeal retrogressive failure likely to have given rise to numerous small-volume collapses. LROC-NAC images M169398317RE and M167043682RE courtesy of NASA/GSFC/ASU.

with myriad individual releases, the deposits are best interpreted as of small-volume flows released onto a mature repose slope.

The considerable runout of the flows, with such uniform narrowness, lack of distinct levee-channel architecture, and ribbon-like parallelism with marked sensitivity to substrate slope, is strongly reminiscent of the trails of laboratory experimental erosion-deposition waves that can move steadily down erodible slopes (see Figure S3) [*Edwards and Gray*, 2015; *Edwards et al*., 2017]. These originate in limited-mass releases that rework the slope, eroding beneath the front of the wave, mixing some wave and substrate material, and progressively depositing material as the tail of the wave passes, leaving a form with a shallow eroded channel and slight levees. From the similarities (discussed further in section 5), we suggest that these striking ribbon-like deposits may be the first known occurrence in nature of the erosion-deposition waves found in the small-scale laboratory experiments. In this scenario, the pronounced dark albedo of the lunar deposits possibly reflects the trail of erosion and mixing of surficial with underlying debris.

3.8. Tralles A Debris Flow Deposits

Debris flow traces and deposits extend ~6 km from rim to floor on the north slope of Tralles A crater, in the highlands north of Mare Crisium (latitude 27.44°N, longitude 73.01°W; Figure 15). The crater age is unknown, although it formed in Imbrian age highlands impact deposits. It is ~18 km in diameter, with a maximum depth of ~3.2 km. Although the wall is extensively degraded, the prominent and stratigraphically upper debris flow deposits have abundant boulders and these also are concentrated in zones where they accumulated from debris fall, so these parts appear younger than 300 Ma. The main slope is remarkably uniform at 32° and runs out onto regolith with darker albedo, sloping from 31° smoothly to ~19°, where the distal deposits terminate.

The degraded crater wall generally slopes with remarkable uniformity for ~4.5 km at 32° and records passage of countless debris flows. The 32° slope must be close to or at the angle of repose of the mass wastage debris, because significant numbers of flows formed very long trails with the main deposit accumulations forming at the slope base. However, the midslope region has myriad short and narrow trails, many of which have no obvious source. These are closely similar to the multiplicity of ribbon-like trails described from Virtanen F crater (Figures 13 and 14) and are here also attributed to erosion-deposition waves resulting from small-volume releases. In this case, however, there is evidence that they can incorporate, transport, and segregate coarse debris, ultimately forming lateral levees. Importantly, these did not form coarse-rich flow terminations, which tends to confirm their formation from waves. Waves can segregate material to the sides, but, lacking any long channelized flow with an upper concentration of coarse material, they do not form any bulbous coarse front.

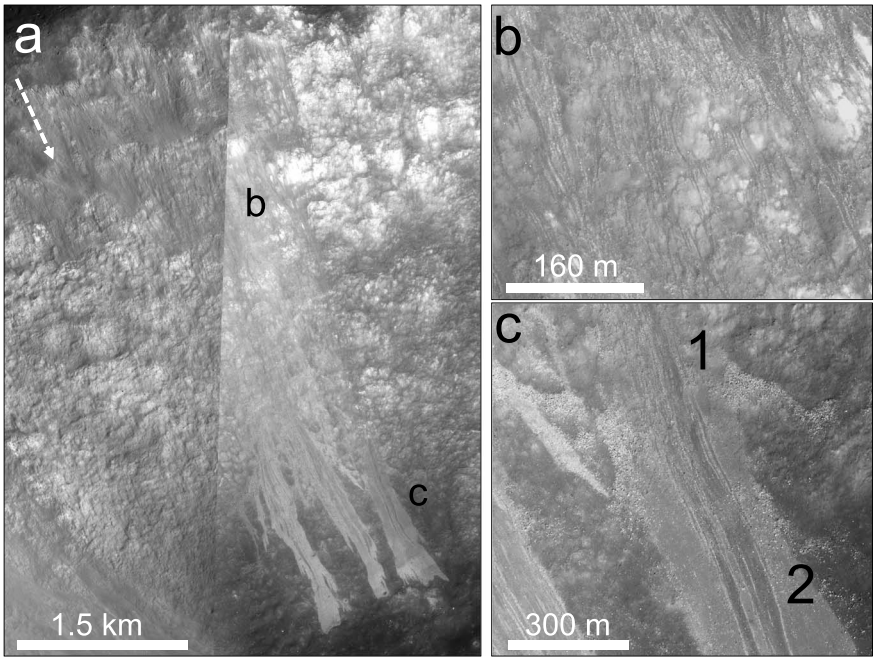

Figure 15. Tralles A crater wall. (a) Entire rim-to-floor extent of debris streaks and more substantial deposits at the slope foot. The crater rim source of many flows shows variably degraded impact craters. Upper slopes, generally at 32°, show extensive degradation with patchy dark-pale albedo showing variable and uneven substrate associated with slight deflection of superimposed trails formed by mainly overpassing debris. (b) Midslopes, also at 32°, show many tens of flow trails, many of which are continuous and have coarse-grained levees, whereas others seemingly start and end with length on the order of hundreds of meters and widths as little as ~4–5 m. Slight deflections of the trails reflect slight topographic unevenness. Transverse zones strewn with boulders are evident. (c) Lower slope at 31° shows that flows entrain and redeposit coarse-boulder accumulations. The dark ribbon-like deposit trails at the site near label 1 lack coarse levees. Lower down these trails evidently cross boulder-strewn zones, where they themselves lack the boulders, while farther down the boulders form distinct levees near the site labeled 2. Evidently, the boulder-poor flows mobilized the coarse material and then segregated it to form lateral levees. LROC-NAC images M111286669RE and M1123292388RE courtesy of NASA/GSFC/ASU.

In section 5 we discuss further the discrimination of wave-formed debris flow deposits from those of the more sustained-flow types.

4. Gravitational and Scale Invariance of Avalanche Fingering

The fingered deposits shown in Figures 10 and 11 are remarkably similar to those in the small-scale laboratory experiments [*Woodhouse et al*., 2012] shown in Figure S5, as well large-scale terrestrial deposits from pyroclastic flows [*Kokelaar et al*., 2014]. One may therefore conjecture that the physical processes that give rise to fingering are both gravitationally and scale invariant. To see how this may arise, we consider conditions under which gravity and spatial lengths may scale out of the governing equations [*Baker et al*., 2016b].

Considerable progress has been made in modeling particle segregation in shallow granular avalanches [*Gray and Thornton*, 2005; *Gray and Chugunov*, 2006; *Gray and Ancey*, 2011, 2015] and especially the preferential transport of large particles toward flow fronts and their accumulation there [*Gray and Ancey*, 2009; *Gray and Kokelaar*, 2010; *Johnson et al*., 2012]. These coarse-grained margins are highly resistive and feed back on the bulk flow causing a uniform front to break down into a series of fingers [*Pouliquen et al*., 1997; *Pouliquen and Vallance*, 1999; *Woodhouse et al*., 2012]. *Baker et al*. [2016b] have developed a well-posed system of equations to model this process in terrestrial systems. The depth-averaged equations that describe these shallow granular flows are derived in a coordinate system that is aligned with the local slope angle θ, and the (x, y) axes point down and across the slope, respectively. The avalanche is integrated through the normal direction to the slope z, and it is assumed to have a bidisperse particle size distribution (i.e., large and small grains).

The model consists of three partial differential equations for the avalanche thickness h, the depth-averaged small particle concentration $\overline{\varphi} \in [0, 1]$, and the depth-averaged velocity $\overline{\boldsymbol{u}}$

$$\frac{\partial h}{\partial t} + \text{div}\,(h\overline{\boldsymbol{u}}) = 0,$$

$$\frac{\partial}{\partial t}(h\overline{\varphi}) + \text{div}(h\overline{\boldsymbol{u}}\overline{\varphi}) - \text{div}((1-\alpha)h\overline{\boldsymbol{u}}\overline{\varphi}(1-\overline{\varphi})) = 0,$$

$$\frac{\partial}{\partial t}(h\overline{\boldsymbol{u}}) + \text{div}\,(h\overline{\boldsymbol{u}}\otimes\overline{\boldsymbol{u}}) + \text{grad}\left(\frac{1}{2}gh^2\cos\theta\right) = gh\,\boldsymbol{S}\cos\theta + \text{div}\left(\nu h^{3/2}\overline{\boldsymbol{D}}\right),$$

where t is time, div and grad are the two-dimensional divergence and gradient operators, $\otimes$ is the two-dimensional dyadic product, g is the gravitational acceleration, and $\overline{\boldsymbol{D}} = \left(\text{grad}\overline{\boldsymbol{u}} + (\text{grad}\overline{\boldsymbol{u}})^{\boldsymbol{T}}\right)/2$ is the two-dimensional depth-averaged strain rate tensor.

The first of these equations is the depth-averaged mass balance equation and implicitly assumes that the avalanche is incompressible. The second equation is the large particle transport equation and describes the process in which large particles segregate to the surface of the avalanche, where the velocity is greatest, and are preferentially transported to the flow front [*Gray and Kokelaar*, 2010]. This equation assumes that the segregation is sufficiently strong that large grains always lie on top of the fines and that there is a linear velocity profile through the avalanche depth, i.e., $\boldsymbol{u}/\overline{\boldsymbol{u}} = \alpha + 2(1-\alpha)z/h$, where the parameter $\alpha \in [0, 1]$ allows it to switch from plug flow ($\alpha = 1$) to simple shear ($\alpha = 0$). The depth-averaged concentration of large particles is $1 - \overline{\varphi}$.

The third equation is the depth-averaged down and cross-slope momentum balance equation. The left-hand side consists of the time rate of change of momentum, momentum transport, and the depth-averaged pressure gradient. The first term on the right-hand side is the depth-averaged source term

$$\boldsymbol{S} = \boldsymbol{i}\,\tan\theta - \mu\left(Fr, \overline{\varphi}, h/\mathscr{L}^L, h/\mathscr{L}^S\right)\frac{\overline{\boldsymbol{u}}}{|\overline{\boldsymbol{u}}|} - \text{grad}\,b,$$

which consists of a component of gravity pulling the avalanche down the slope in the $\boldsymbol{i}$ direction, a frictional resistance term μ, which assumes a rough bed friction law [*Pouliquen*, 1999; *Pouliquen and Forterre*, 2002; *Woodhouse et al.*, 2012] that is dependent on the Froude number

$$Fr = \frac{|\overline{\boldsymbol{u}}|}{\sqrt{gh\cos\theta}},$$

the depth-averaged small particle concentration $\overline{\varphi}$, as well as the ratios $h/\mathscr{L}^L$ and $h/\mathscr{L}^S$, where $\mathscr{L}^L$ and $\mathscr{L}^S$ are length scales for the frictional transition for the large and small particles, respectively [*Pouliquen and Forterre*, 2002]. These length scales are a property of the particle shape, size, and surface, as well as of the bed that it flows over. The source term also includes the effect of shallow changes in topography through gradients in the height $z = b(x, y)$; see *Gray et al.* [1999] and *Viroulet et al.* [2017].

The final term on the right-hand side of the momentum balance equation is a viscous-like term that is derived by depth averaging the $\mu(I)$-rheology for granular flows [*Jop et al.*, 2006]. *Gray and Edwards* [2014] showed that for a monodisperse flow the depth-averaged viscosity is equal to $\nu^c h^{1/2}/2$, where the coefficient

$$\nu^c = \frac{2}{9}\frac{\mathscr{L}^c\sqrt{g}}{\beta}\frac{\sin\theta}{\sqrt{\cos\theta}}\left(\frac{\tan\theta_2^c - \tan\theta}{\tan\theta - \tan\theta_1^c}\right).$$

Pure phases of large and small particles will obey this law, and the constituent superscripts $c = L, S$ are therefore used to indicate that a variable relates to large or small particles, respectively. In this equation the nondimensional parameter β is a proportionality factor in Pouliquen's [1999] rough bed friction law, and θ_2^c and θ_1^c are the upper and lower angles for the existence of steady uniform flows for constituent c. It is important to note that some form of regularization is required if the slope inclination lies outside the range $\theta_1^c < \theta \le \theta_2^c$ to prevent the viscosity becoming negative. The effective viscosity of a mixture of particles is a matter of current research. However, in the first instance it is reasonable to assume that the coefficient ν in the mixture viscosity $\nu\, h^{1/2}/2$ is a depth-averaged volume fraction weighted average of the coefficients of the pure phases, i.e.,

$$\nu = \overline{\varphi}\nu^S + (1-\overline{\varphi})\nu^L.$$

To examine the effect of gravity and flow size, one can nondimensionalize the equations by the scalings

$$(x, y, h, \mathscr{L}^L, \mathscr{L}^S, b) = H\left(\tilde{x}, \tilde{y}, \tilde{h}, \widetilde{\mathscr{L}^L}, \widetilde{\mathscr{L}^S}, \tilde{b}\right), \qquad \overline{\boldsymbol{u}} = \sqrt{Hg}\,\widetilde{\overline{\boldsymbol{u}}}, \qquad \overline{\boldsymbol{D}} = \sqrt{\frac{g}{H}}\,\widetilde{\overline{\boldsymbol{D}}},$$

$$(\nu, \nu^L, \nu^S) = H\sqrt{g}\,\left(\tilde{\nu}, \tilde{\nu^L}, \tilde{\nu^S}\right) \qquad t = \sqrt{H/g}\,\tilde{t},$$

where H is a common length scale that may be related to the mean grain size or the typical avalanche thickness, and the tilde indicates a nondimensional variable [*Gray and Edwards*, 2014]. Substituting these into the three partial differential equations, it follows that they become

$$\frac{\partial \tilde{h}}{\partial \tilde{t}} + \widetilde{\operatorname{div}}\left(\tilde{h}\,\widetilde{\overline{\boldsymbol{u}}}\right) = 0,$$

$$\frac{\partial}{\partial \tilde{t}}\left(\tilde{h}\overline{\varphi}\right) + \widetilde{\operatorname{div}}\left(\tilde{h}\widetilde{\overline{\boldsymbol{u}}}\overline{\varphi}\right) - \widetilde{\operatorname{div}}\left((1-\alpha)\tilde{h}\widetilde{\overline{\boldsymbol{u}}}\overline{\varphi}(1-\overline{\varphi})\right) = 0,$$

$$\frac{\partial}{\partial \tilde{t}}\left(\tilde{h}\widetilde{\overline{\boldsymbol{u}}}\right) + \widetilde{\operatorname{div}}\left(\tilde{h}\widetilde{\overline{\boldsymbol{u}}}\otimes\widetilde{\overline{\boldsymbol{u}}}\right) + \widetilde{\operatorname{grad}}\left(\frac{1}{2}\tilde{h}^2\cos\theta\right) = \tilde{h}\boldsymbol{S}\cos\theta + \widetilde{\operatorname{div}}\left(\tilde{\nu}\tilde{h}^{3/2}\widetilde{\overline{\boldsymbol{D}}}\right),$$

where $\widetilde{\operatorname{div}}$ and $\widetilde{\operatorname{grad}}$ are the nondimensionalized two-dimensional divergence and gradient operators. These equations are completely independent of the gravitational acceleration g and the spatial scale H, as are the source term

$$\boldsymbol{S} = \boldsymbol{i}\,\tan\theta - \mu\left(Fr, \overline{\varphi}, \tilde{h}/\widetilde{\mathscr{L}^L}, \tilde{h}/\widetilde{\mathscr{L}^S}\right)\frac{\widetilde{\overline{\boldsymbol{u}}}}{\left|\widetilde{\overline{\boldsymbol{u}}}\right|} - \widetilde{\operatorname{grad}}\tilde{b},$$

the Froude number $Fr = \left|\widetilde{\overline{\boldsymbol{u}}}\right|/\sqrt{\tilde{h}\cos\theta}$, the coefficients

$$\tilde{\nu^c} = \frac{2}{9}\frac{\widetilde{\mathscr{L}^c}}{\beta}\frac{\sin\theta}{\sqrt{\cos\theta}}\left(\frac{\tan\theta_2^c - \tan\theta}{\tan\theta - \tan\theta_1^c}\right), \qquad c = L, S,$$

and their concentrated weighted average

$$\tilde{\nu} = \overline{\varphi}\tilde{\nu^S} + (1-\overline{\varphi})\tilde{\nu^L}.$$

Since gravity g completely scales out of the problem, in a reduced gravity environment, such as on the Moon, the debris flow fingers will have exactly the same morphology as on Earth, although the flow velocity will be reduced and the timescale to reach the final configuration will be correspondingly increased. This reduction/enhancement factor is proportional to the square root of the gravitational acceleration.

The nondimensionalization also implies that H scales out of the problem as well. It follows that if everything is scaled up proportionately, the fingering will be the same. This quite remarkable result explains why there is such an amazing similarity between the small-scale laboratory experiments (Figure S5) [*Pouliquen et al*., 1997; *Felix and Thomas*, 2004; *Woodhouse et al*., 2012] and the Moon deposits as depicted in Figures 10 and 11. This result relies on the very special forms of Pouliquen and Forterre's [2002] friction law, the depth-averaged viscous terms from the $\mu(I)$-rheology [*Gray and Edwards*, 2014; *Baker et al*., 2016c], and the large particle transport equation [*Gray and Kokelaar*, 2010]. The big assumption in this argument is that the frictional length scales $\mathscr{L}^L$ and $\mathscr{L}^S$ scale with the length scale H. Since H may be related to the mean grain size in the avalanche, which is much larger on the Moon than it is in the small-scale experiments, one may therefore anticipate much larger fingering length scales on the Moon. The apparent scale invariance may also in part be a reflection of the fact that the substrate on the Moon is formed from an erodible layer rather than a fixed bed in the laboratory experiments, which also implies that $\mathscr{L}^L$ and $\mathscr{L}^S$ will be larger on the Moon. If, on the other hand, $\mathscr{L}^L$ and $\mathscr{L}^S$ do not scale with H, then the whole argument breaks down and both the effective basal friction μ and the effective viscosity $\nu\, h^{1/2}/2$ do not scale up and the morphology of the deposit will be different. In this case fingers might still form, but they will have different scaling properties.

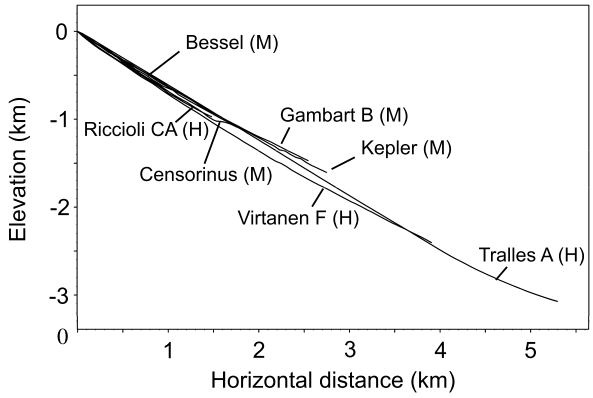

Figure 16. Debris flow deposit profiles, extending from source(s), normalized to same starting height, to distal termination. Suffixes (M) and (H) indicate mare and highland substrates, respectively. Although Virtanen F and Tralles A have exceptional runout, the highland crater slope angles do not distinguish them from the mare examples. The Censorinus profile shows the abrupt slope change to ~25° near the deposit terminal accumulation.

This gravitational and scale invariance also applies to erosion-deposition waves [*Edwards and Gray*, 2015; *Edwards et al*., 2017], which use exactly the same form of equations but are not reliant on mobility feedback due to segregation. These invariance results significantly extend those for dry granular avalanches with constant Coulomb basal friction [*Savage and Hutter*, 1989] and show that segregation induced fingering and the erosion-deposition waves may potentially explain many features on a wide range of planetary bodies.

5. Discussion

5.1. Comparison With Terrestrial Analogues

Morphologies of lunar mass wastage deposits are, with some exceptions, mostly similar to those seen on Earth in nature and in laboratory experiments, at both large and small scales; some forms are reproducible in numerical simulations [e.g., *Lube et al*., 2007; *Kokelaar et al*., 2014; *Baker et al*., 2016a, 2016b]. The morphological similarities reflect the fact that there is no fundamental influence of the reduced gravity on flow behavior (section 4), and the exceptions are thus most likely to relate to material differences. Granular segregation is widely evident on the Moon and, as on Earth, predominantly longitudinal in debris fall deposits and both longitudinal and lateral in debris flow deposits. LROC images do not permit discrimination of subboulder grain sizes, but material fragmentation within craters, both at the surface (due to space "weathering") and within avalanches, inevitably must produce sand-grade and finer sediment (≤2 mm). Such fines will tend to segregate downward and lag behind coarser material in both debris falls and debris flows [e.g., *Kokelaar et al*., 2014, Figure 5], so we infer that this is probably an abundant constituent of the diffuse streaks on relatively steep slopes and in the pale surficial material impounded behind coarse levees (Figures 4 and 5). Our further inference that the pale fringes in front of coarse-grained flow deposit terminations (Figures 5 and 11) are mainly of fines that drained through the coarse deposits, however, warrants further consideration. Strictly, the pale fringes have no natural terrestrial counterpart.

On Earth, dry avalanches tend to elutriate fines upward to form local suspension clouds by expulsion of trapped air [*Hsü*, 1975; *Köhler et al*., 2016] and, thus, form fallout deposits, but there is no suspending medium on the Moon and charging-related segregation seems unlikely at the scale of the fringes. Also, the possibility that the enigmatic fringes could arise from collisions during flow, with essentially ballistic particle ejection and fallout, seems unlikely according to their apparent thickness and the dense (only slightly dilated) nature of the flow. On Earth, fines are commonly washed out by water draining from the coarse peripheries of wet debris flow deposits [e.g., *Kokelaar et al*., 2014, Figure 2], but clearly this cannot be the case on the Moon. However, hourglass-like gravitational draining of dry fines between coarse marginal fragments seems highly likely where the fines were built high behind a steep front [*Kim and Lowe*, 2004]. The fringes seem best developed in front of steep lobate debris flow deposits that clearly have impounded fines and where a slope allowed the sand to flow a little farther.

A special feature of the Moon is the existence of impact craters with inner slopes that are dominated by dry granular materials and, from frictional freezing of debris flows, are widely close to their dynamic angle of stable repose (Figure 16). The catastrophic mass wasting of crater walls that immediately followed their formation is poorly known, because the earliest deposits are mostly buried beneath products of subsequent lesser mass-wasting events and now we only observe the uppermost products of those. The main consequences of the occurrence of avalanches on long-exposed slopes close to their dynamic angle of repose are that (1) erodible fines are likely to be involved, (2) most midslope regions are characterized by material overpassing, marked by some erosion and little deposition, and (3) granular erosion-deposition waves can propagate

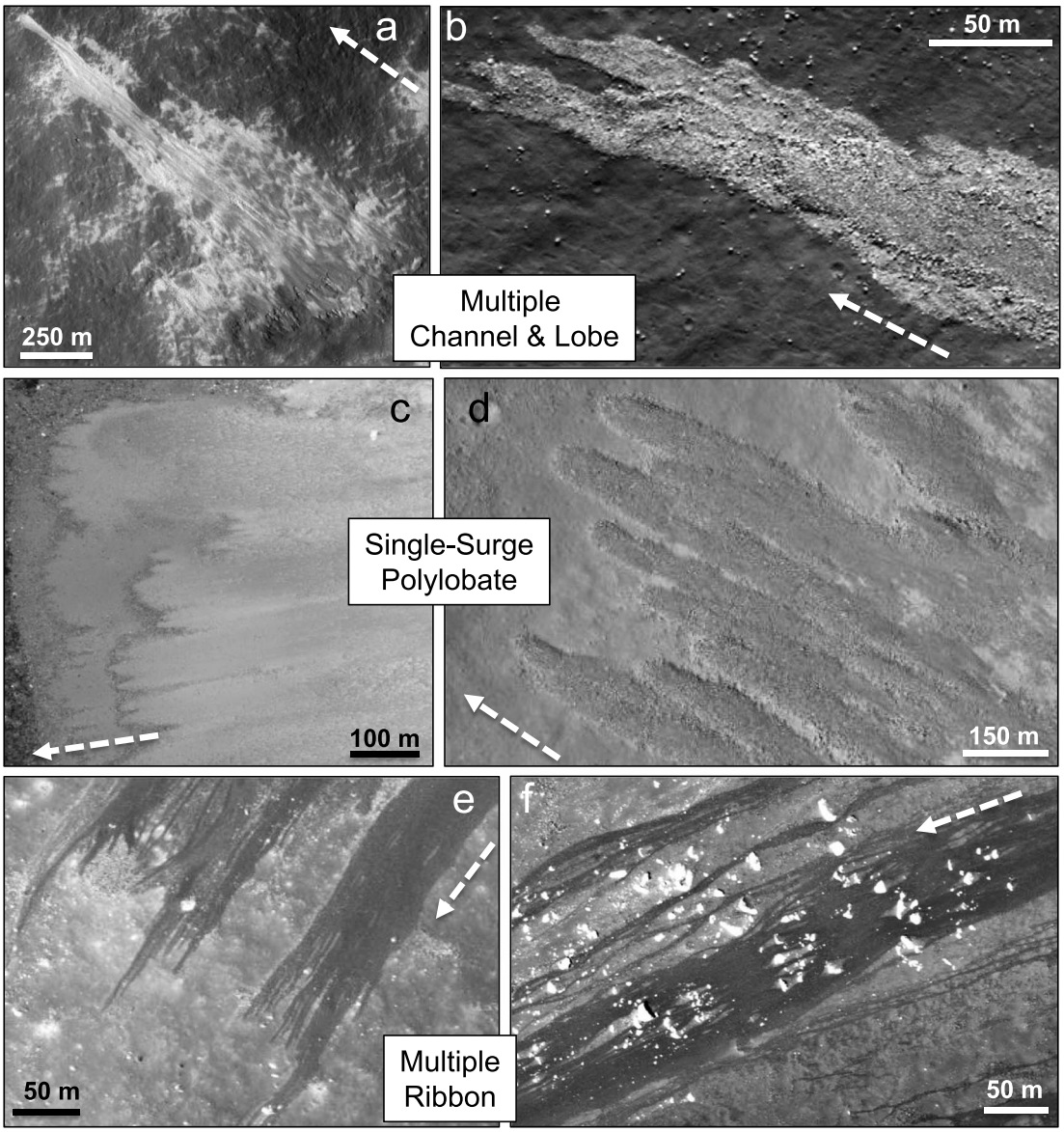

Figure 17. Flow deposit types. Multiple channel and lobe type is exemplified by (a) Riccioli CA (see section 3.6) and (b) Gambart B (see section 3.3), single-surge polylobate type is exemplified by (c) Censorinus (see section 3.5) and (d) Bessel (see section 3.4), and multiple-ribbon type is exemplified by (e and f) Virtanen F (see section 3.7).

considerable distances. The Moon, unlike Earth, shows common occurrence of relatively small-volume deposits that record long-distance runout of dry granular flows (Table 2), widespread occurrence of remobilization of coarse debris due to their inundation with fines, and instances of peculiar ribbon-like flow trails of kilometer lengths and few-meter widths.

5.2. Discrimination of Flow Deposit Types

This study finds three main types of debris flow deposit (Figure 17). Relative frequency of their occurrence in general is unknown, because we have studied only a very few craters that have been imaged to high spatial resolution and deposits that are well preserved (i.e., young and fresh).

5.2.1. Multiple Channel and Lobe Type

Multiple-channel and lobe debris flow deposits are typified by examples in Gambart B and Riccioli CA craters. The type is the most common in our study, recording multiple small-volume flows that originate piecemeal in clusters of small cliffs and form variably intersecting coarse-leveed channels that tend to drain on steeper

slopes and terminate at mounded accumulations of coarse debris that impounds finer debris. Closely similar channel-levee morphology with channel draining and lobate coarse deposit terminations is readily produced in experiments in which the unmixing (segregation) of polydisperse granular mixtures is remarkably rapid [e.g., *Kokelaar et al*., 2014] (Figures S1 and S2). Irregular-shaped fingers and overlapping terminations are typical, widely with evidence that following flows used preexisting channels and broke through the terminations of predecessor deposits. Gambart B and Riccioli CA craters are, respectively, in mare and highland settings, and we find no obvious difference related to setting for this type, either in slope angle (Table 2 and Figure 16) or deposit architecture, but our sample set is insufficient for a robust conclusion. Kepler crater has several examples of this type (e.g., the "early flow deposits" of Figure 5b), although the source regions and full runouts there are unknown. Multiple channel and lobe (MCL)-type deposits are closely similar in form to deposits of debris flows on Earth, which typically involve interstitial water and, seemingly in contrast to the dry Moon, can display considerable low-slope runout [e.g., *Legros*, 2002]. We consider avalanche runout in section 5.4.

5.2.2. Single-Surge Polylobate Type

This type is typified by examples in Bessel and Censorinus craters. Characteristic features are the parallelism and close granular and form similarities of numerous undrained lobes or fingers that reflect growth from the regular periodic frontal instability of a single advancing polydisperse mass (Figure S5). In contrast to the other types, these debris flow deposits appear to record relatively large-volume mass wasting that involves simultaneous collapse of extensive source regions. The characteristic features are most unlikely to form from numerous, piecemeal, smaller collapses. The single-surge polylobate (SSP)-type deposit volumes relative to the other types (Table 2) confirm the involvement of relatively large avalanches. Where this type forms with a limited frontal width, the lobes and fingers tend to splay and form cat's paw-like morphology on diminished slopes. The Kepler site has relatively small examples similar to this type (Figure 5a), with low slopes having cat's paw forms traceable to drained channels farther upslope (Figure 4c). The Kepler coarse deposits manifestly impound finer sediment and are interpreted (section 3.2.2) as resulting from fine debris incursions over coarse talus that became remobilized. Characteristic of this SSP type, the Kepler lobate forms seemingly register singular advances of polydisperse, segregating flows.

5.2.3. Multiple-Ribbon Type

This type is typified by examples in Virtanen F and Tralles A craters. The characteristics are extreme length-to-width ratios, commonly kilometers length and a few meters width, persistent ribbon-like parallelism of margins that generally lack obvious levees, absence of mounded coarse-grained terminations, and considerable sensitivity to slope changes. Where the slope is slightly irregular the tracks curve and can become braided, but otherwise extensive subparallelism is typical. The characteristics of these ribbon-like flow deposits are strikingly similar to those of experimental granular waves (Figure S3), and they are here interpreted as registering passage of erosion-deposition waves [*Edwards and Gray*, 2015; *Edwards et al*., 2017] down erodible slopes at or near the dynamic repose angle of the substrate material. Characteristic of the experimental flows is their extreme sensitivity to slope changes, with successive waves normally unable to surmount previous slight levees. This tallies with the ribbon-like deposits that separate and rejoin on the slope above and below slight substrate elevations where there are large boulders (not due to the boulders themselves).

Multiple small collapses at source each apparently trigger granular waves that advance considerable distances by reworking with mixing of the slope deposits. Similar but shorter trails, commonly with no obvious input source, occur on slopes near the major multiple units. Some flows that form multiple-ribbon (MR)-type deposits evidently entrain and redistribute boulder-rich debris that they encounter in their path. The Tralles A crater instances (Figure 15c) show that incorporated boulders are segregated to form lateral levees, but, unlike the other deposit types, there are no coarse-grained mounded accumulations at the flow-deposit terminations. This is consistent with reworking by waves, because waves do not involve elongate channelized flow that segregates and streams coarse debris to accumulate at the flow front.

The common dark albedo of the flow tracks, which in many instances show no obvious topographic relief, is attributed to erosion, mixing, and redeposition of slope substrate during passage of waves. We infer that the pale substrate is mainly fine-grained regolith with underlying less degraded debris. Thus, the dark tracks may be mixed and redeposited material that is somewhat coarser and less smooth and appears darker than adjacent surface materials. Steadily advancing and nonbulking erosion-deposition waves typically tend only to leave slight levee-channel morphology, except where entrained coarse material is dumped to the sides.

These multiple-ribbon-type debris flow deposits and associated tracks that we interpret as due to the passage of granular erosion-deposition waves are the first reported instances of their occurrence in nature on any planetary body. The exceptional runout length of what must have been relatively small-volume flows, and their restriction in our study to lunar highlands sites, begs some consideration and probably further exploration too. We are unaware of any closely similar natural flow-deposit type on Earth, and our laboratory experiments using pure sand (Figure S3) barely reflect the kilometers of runout that has occurred on the Moon.

As there is no fundamental influence of the lunar reduced gravity on flow behavior (section 4), the special presence on the Moon of MR-type flow deposits suggests special material conditions rather than any different physics. The midslopes of the highland Virtanen F and Tralles A sites of the MR-type deposits appear similar to mare crater slopes, at ~32° (Table 2 and Figure 16), so it seems possible that the generally finer grain size of highlands regolith, with median size 37.5 μm rather than 60 μm [*McKay et al*., 1974], together with the unusual low density (<1 g/cm^3) and hence loose packing, render the long highlands slopes particularly suited to transmission of granular erosion-deposition waves that travel "through and along" the repose layer. The other highland site we studied, Riccioli CA, has a slightly steeper midslope, at ~34°, but the avalanche there appears to have contained abundant coarse debris. With such a limited data set, we can only speculate that the MR-type flows are dominantly of relatively fine regolith interacting with fine regolith on slopes close to repose and that they are not formed from flows dominantly of coarse grains.

Speculatively, erosion-deposition waves may be favored on the Moon (1) by the abundance of relatively fine (i.e., boulder-free) material at repose angle, (2) by the relatively low gravity (0.16 *g*), which facilitates granular dilation [*Kleinhans et al*., 2011], and (3) by the lack of interstitial fluid. A granular wave front has to dilate the deposit it necessarily mobilizes (erodes) to flow, and this is likely to be "easier" in a vacuum, as the necessary dilation does not have to work against any viscous drag of drawn-in ambient fluid.

It is impossible to discover even the approximate original granulometry of the lunar flows and their deposits, although coarse-fine granular segregation evidently occurred in flows that produced deposit types MCL and SSP, and the Tralles A MR-type deposits clearly show that some active unmixing occurred. Granular segregation that can feed back onto flow runout behavior will occur rapidly in polydisperse flows that may have only a limited grain size range and involve a coarse component far too small to resolve by the LROC-NAC imaging. Thus, we are unable to refine our crude classification of flow-deposit types, which are end-members between which there are likely to be various transitional types. For example, some narrow fan-like deposit piles have uppermost layers with irregular, somewhat lobate coarse terminations that have fines on top and lack drained channels just behind them [see *Kumar et al*., 2013, Figure 3]. These may be broadly transitional between MCL and SSP flow types, resulting from moderate-volume multiple flows constrained to flow through gullies and thereafter rapidly spreading and depositing.

5.3. Effects of Rock Type and Grain Size

In our limited study of equatorial lunar regions, we found no clear influence of crater target rock type—mare versus highlands—on the granular-slope angles. All of the studied slopes on which there are debris flow deposits are composed of previously deposited granular material and are closely similar. The midslope angles reported in Table 2 and Figure 16 generally represent a zone where there has been significant overpassing of debris, in some cases extending for several kilometers. Lower down there is commonly evidence of tendency to deposit, and above there may be a steeper zone where alcoves and gullies have been eroded [*Kumar et al*., 2013]. As is normal with deposit cones and aprons, the slopes tend to lessen gradually downward. All of the studied slopes have aggraded through their extreme long-term evolution by mass wasting to have their main midslope reaches between 31.5° and 34°, close to or slightly less than the critical static repose angle for dry sand on Earth, which is ~34°. This small difference could merely be the difference between the dynamic and static friction angles and/or due to abundance of fines 60 μm or finer and/or due to the reduced gravity. Given the uncertainties regarding the lunar sediment makeup, we have no way of refining this and, strictly, find no really significant difference to Earth. We expect that all lunar debris flows in ancient craters in nonpolar regolith environments will have had a significant content of fine-grained regolith, involved at source and/or erosionally incorporated in traversing the mature crater slopes. There is no evidence that reflects any cohesive/adhesive effects of the fines. The apparent remobilization of coarse talus residing on ledges, as a result of inundation there by boulder-free material, does suggest some friction reduction effect of regolith fines in the flows in general.

5.4. Avalanche Runout

Many avalanches on Earth extend surprisingly large distances on low and adverse slopes. This phenomenon is not clearly apparent for the Moon, where extensive low-slope flow deposits are rare and their origin(s) uncertain and conceivably impact surge related [*Howard*, 1973; *Legros*, 2002; *Robinson and Jolliff*, 2002]. Indeed, this paucity of low-slope flow deposits on the Moon has been taken to indicate that water (pore water pressure) [*Iverson*, 1997] is a key factor in the extreme mobility of wet flows on Earth [*Legros*, 2002], while for dry flows on Earth friction reduction by interstitial fluid, such as dusty gas [*Hsü*, 1975], and/or acoustic fluidization [*Melosh*, 1979; *Johnson et al*., 2016] has been invoked. Our findings of long runout of dry-debris flows on the Moon simply relate to the very long granular slopes close to repose angles that occur there, unlike on Earth. In our limited sample set of flow deposits, we find no low-slope runout and, thus, no evidence for occurrence of any special mechanism(s) for reduction of granular friction. Our study reveals numerous instances of dense frictional debris flows that stopped with deposition on near-repose-angled slopes (Figure 4c), and in general most flow deposit terminations lie on slopes only a few degrees less than where there was substantial material overpassing (Figure 16). If the extensive (21 km^2), thin (<20 m) low-slope "Bright Landslide Deposit" (also known as "light mantle") of the Apollo 17 site does record a large-volume low-slope avalanche from a nearby mountain, triggered by impacts [*Howard*, 1973; *Hurwitz and Kring*, 2016] or seismic shaking [*Schmitt et al*., 2017], then flow across, and incorporation of, highly erodible and porous regolith [*Mangeney et al*., 2010] seems likely to be implicated.

6. Conclusions

Granular flow processes on the Moon are similar to those on Earth. Reduced gravity (0.16 *g*) serves to reduce flow speed and hence increase its duration; any possible slight enhancement of flow mobility [*Kleinhans et al*., 2011] is not detectable. Theoretical scale invariance can explain the remarkable similarity of deposits on the Moon and Earth, including the small-scale laboratory experiments (Figures S1–S5). This is especially important for our new inference of granular erosion-deposition waves in accounting for exceptional (up to kilometers) runout related to small-volume initial slope failures. The considerable runout distances of dry lunar debris flows in general simply reflect the great lengths of granular slopes close to repose angle on the Moon. Highland terrain slopes with regolith close to repose angle may favor the occurrence on them of the hypothesized erosion-deposition waves; otherwise we find no clear distinction between mass wasting in either mare or highlands equatorial craters. We find that the modal dynamic angle of repose is between ~31.5° and 34°, slightly less than the ~36° reported by *Wagner et al*. [2013] for small (<20 km) Copernican craters, which perhaps included slopes closer to flow sources than our "midslope" measures.

The main control of flow deposit type formed from mass wasting on the Moon relates to the amount of mass released in a single event and to the material grain size distribution. Small, coarse-boulder-rich flows tend to produce multiple channel and lobe (MCL-type) deposits that record unsteady flow advance. More substantial collapses of similar material form more uniform deposits, with characteristic parallel fingers and lobes on a self-similar spatial scale (SSP-type), reflecting flow advance and segregation of a single mixed-particle (polydisperse) mass with evolving frontal instability. Multiple-ribbon-like deposits that are outstandingly long for the apparent amount of flowing material (MR-type) record flows primarily of boulder-free material on fine erodible substrate at or close to repose. We propose that these flows can be triggered by limited-volume mass wasting and then propagate as one or more granular waves, with the cycle of erosion-deposition continuously involving preexisting slope material such that the initial singular mass release acts to rework the slope far beyond its own material extent. The deposit is mainly formed from reworked slope material and its volume, thus, may have little direct relation to the initiating slope disturbance. Further studies are warranted to learn more about the controls of occurrence of dry granular erosion-deposition waves and the extent(s) to which they may mix substrate deposits and alter slope albedo.

We have described evidence from which we infer three previously unrecognized dry-debris flow phenomena: (1) remobilization of stable coarse talus by inundation with relatively fine debris deduced to contain a significant proportion of grains ≤2 mm; (2) draining-related development of veils of such fine debris around the coarse-grained peripheries of some coarse-fine segregated flow deposits; and (3) occurrence of long-runout erosion-deposition waves. None of these is fully understood, but granular experiments and our scaling arguments do provide compelling support for our inferences. Our most important hypothesis concerns the

occurrence of long-runout dry granular waves. The lunar multiple-ribbon-type deposits have highly distinctive characteristics that should make them recognizable elsewhere where long repose-angled slopes of fine dry debris have formed, such as on Mars. The lunar ribbon deposits bear some pattern resemblances to the ephemeral, terminally fingering dark slope streaks on Mars [e.g., *Sullivan et al*., 2001], attributed mostly to dust avalanches there. They too record gravity-driven flows susceptible to topographic deflection, but they splay distally and fade with time, older ones becoming paler, and they would not sweep and redistribute boulders they encountered.

7. Planetary Science Applications

Lunar avalanches only involve dry granular movement. Thus, this study benchmarks, in new detail, what flow processes and flow-deposit morphologies occur in the absence of liquid and gas and without reworking due to them. More widely, granular avalanches are a key comparative planetary process and their deposits on planetary surfaces should be considered important targets for further study and future exploration to fully understand their sedimentological evolution and activation trigger(s). The presence or absence of atmospheres and their differing phases of surface volatiles may influence and yield contrasting mass-wasting processes and deposits on other planetary bodies including Mars (i.e., "gullies" and recurring slope lineae) [*Treiman*, 2003; *Barnouin-Jha et al*., 2005; *Bart*, 2007; *McEwen et al*., 2014; *de Haas et al*., 2015; *Schmidt et al*., 2017], Mercury [*Brunetti et al*., 2015], asteroid 4 Vesta [*Otto et al*., 2013; *Krohn et al*., 2014; *Williams et al*., 2014] and even comet 67P/Churyumov-Gerasimenk [*Pajola et al*., 2017]. Additionally, the potential effect of extreme diurnal or other temperature variations on granular movement warrants consideration [e.g., *Molaro and Byrne*, 2012; *Molaro et al*., 2017].

From a mission-planning perspective, mass wastage deposits are attractive exploration sites that enable the study and/or collection of a wide "suite" of geological material sourced from a variety of distal source region(s) now colocated within a localized geographic setting. These deposits could provide the only (albeit indirect) sampling of outcrops located upslope on steep crater wall cliff settings [e.g., see *Kickapoo Lunar Research Team and Kramer*, 2014], providing stratigraphic sampling of otherwise inaccessible terrains. Such targeted sampling of debris flow deposits and boulders proved scientifically valuable during crewed geological exploration of the Apollo 17 landing site (see section 5.4) [*Hurwitz and Kring*, 2016] and has been proposed as a strategy that should be employed during future integrated human and robotic exploration of the lunar surface [e.g., *Potts et al*., 2015; *Steenstra et al*., 2016]. Sampling of planetary debris flow deposits, thus, provides opportunistic sampling sites that potentially could reduce the necessity for long-duration surface mobility in mission-planning design and/or provide a rewarding geological sampling stop during a time-pressured crewed extravehicular traverse. Further understanding of the geological context and form of granular avalanche deposits on the Moon and other planetary surfaces necessitates utilizing high-resolution orbital image data to maximize the science potential of such future mission-planning activities.

Acknowledgments
B.P.K. and J.M.N.T.G. acknowledge assistance of Romaine Graham, James Vallance, and Mark Woodhouse in some laboratory experiments and support from NERC grants NE/E003206/1 and NE/K003011/1. J.M.N.T.G. is a Royal Society Wolfson Research Merit Award holder (WM150058) and an EPSRC Established Career Fellow (EP/M022447/1). R.B. was supported by an STFC studentship awarded to the University of Manchester, and K.H.J. acknowledges STFC grant ST/M001253/1 and Royal Society grant RS/UF140190. S.V. acknowledges support from NERC grant NE/K003011/1. R.B. acknowledges technical assistance from Kofi Owusu and Karl Hennermann. USGS PILOT converted IMG. files into .cub files readable in ArcMap, and Lisa Gaddis and Trent Hare advised on processing LROC data. The "Virtual Moon Atlas" was utilized for this project. All research data supporting this publication are directly available within this publication or from the NASA Planetary Data System (see text for image details). We thank two anonymous reviewers for their detailed and insightful reviews that helped to improve the manuscript and Steven Hauck for editorial handling.

References

Arnold, J. R. (1979), Ice in the lunar polar regions, *J. Geophys. Res.*, *84*, 5659–5668, doi:10.1029/JB084iB10p05659.
Baker, J. L., T. Barker, and J. M. N. T. Gray (2016a), A two-dimensional depth-averaged $\mu(I)$-rheology for dense granular avalanches, *J. Fluid Mech.*, *787*, 367–395.
Baker, J. L., J. M. N. T. Gray, and B. P. Kokelaar (2016b), Particle size-segregation and spontaneous levee formation in geophysical granular flows, *Int. J. Erosion Control Eng.*, *9*, 174–178.
Baker, J. L., C. G. Johnson, and J. M. N. T. Gray (2016c), Segregation-induced finger formation in granular free-surface flows, *J. Fluid Mech.*, *809*, 168–212.
Bandfield, J. L., E. Song, P. O. Hayne, B. D. Brand, R. R. Ghent, A. R. Vasavada, and D. A. Paige (2014), Lunar cold spots: Granular flow features and extensive insulating materials surrounding young craters, *Icarus*, *231*, 221–231.
Barker, M. K., E. Mazarico, G. A. Neumann, M. T. Zuber, J. Haruyama, and D. E. Smith (2016), A new lunar digital elevation model from the lunar orbiter laser altimeter and SELENE terrain camera, *Icarus*, *273*, 346–355.
Barnouin-Jha, O. S., S. Baloga, and L. Glaze (2005), Comparing landslides to fluidized crater ejecta on Mars, *J. Geophys. Res.*, *110*, E04010, doi:10.1029/2003JE002214.
Bart, G. D. (2007), Comparison of small lunar landslides and Martian gullies, *Icarus*, *187*, 417–421.
Bart, G. D. (2014), The quantitative relationship between small impact crater morphology and regolith depth, *Icarus*, *235*, 130–135.
Bart, G. D., R. D. Nickerson, M. T. Lawder, and H. J. Melosh (2011), Global survey of lunar regolith depths from LROC images, *Icarus*, *215*, 485–490.
Basilevsky, A. T., J. W. Head III, and F. Hörz (2013), Survival times of meter-sized boulders on the surface of the Moon, *Planet. Space Sci.*, *89*, 118–126, doi:10.1016/j.pss.2013.07.011.
Basilevsky, A. T., M. A. Kreslavsky, I. P. Karachevtseva, and E. N. Gusakova (2014), Morphometry of small impact craters in the Lunokhod-1 and Lunokhod-2 study areas, *Planet. Space Sci.*, *92*, 77–87.

Brunetti, M. T., Z. Xiao, G. Komatsu, S. Peruccacci, and F. Guzzetti (2015), Large rock slides in impact craters on the Moon and Mercury, *Icarus*, *260*, 289–300.
Campbell, B. A., J. F. Bell III, S. H. Zisk, B. R. Hawke, and K. A. Horton (1992), A high-resolution radar and CCD imaging study of crater rays in Mare Serenitatis and Mare Nectaris, Proc. 22nd Lunar Planet. Sci. Conf., 259–274.
Canup, R. M. (2012), Forming a moon with an Earth-like composition via a giant impact, *Science*, *338*, 1052–1055.
Canup, R. M., and E. Asphaug (2001), Origin of the Moon in a giant impact near the end of Earth's formation, *Nature*, *412*, 708–712.
Carrier, W. D., III (1973), Lunar soil grain size distribution, *Moon*, *6*, 250–263.
Carrier, W. D., III (2003), Particle size distribution of lunar soil, *J. Geotech. Geoenviron.*, *129*, 956–959.
Carrier, W. D., III, G. R. Olhoeft, and W. Mendell (1991), Physical properties of the lunar surface, in *Lunar Sourcebook*, edited by G. Heiken, D. Vaniman, and B. M. French, pp. 475–594, Cambridge Univ. Press, New York.
Carrigy, M. A. (1970), Experiments on the angles of repose of granular materials, *Sedimentology*, *14*, 147–158.
Chen, H., Y. L. Liu, X. Q. Zhao, and Y. Liu (2015), Numerical investigation on angle of repose and force network from granular pile in variable gravitational environments, *Powder Technol.*, *283*, 607–617.
Colwell, J. E., S. Batiste, M. Horányi, S. Robertson, and S. Sture (2007), Lunar surface: Dust dynamics and regolith mechanics, *Rev. Geophys.*, *45*, RG2006, doi:10.1029/2005RG000184.
Corsini, A., L. Borgatti, F. Cervi, A. Dahne, F. Ronchetti, and P. Sterzai (2009), Estimating mass-wasting processes in active Earth slides—Earth flows with time-series of high-resolution DEMs from photogrammetry and airborne LiDar, *Nat. Hazards Earth Syst. Sci.*, *9*, 433–439.
de Haas, T., E. Hauber, S. J. Conway, H. van Steijn, A. Johnsson, and M. G. Kleinhans (2015), Earth-like aqueous debris-flow activity on Mars at high orbital obliquity in the last million years, *Nat. Commun.*, *6*, doi:10.1038/ncomms7543.
Delbo, M., G. Libourel, J. Wilkerson, N. Murdoch, P. Michel, K. T. Ramesh, C. Ganino, C. Verati, and S. Marchi (2014), Thermal fatigue as the origin of regolith on small asteroids, *Nature*, *508*, 233–236.
Deplus, C., A. Le Friant, G. Boudon, J.-C. Komorowski, B. Villemant, C. Harford, and J.-L. Cheminée (2001), Submarine evidence for large-scale debris avalanches in the Lesser Antilles Arc, *Earth Planet. Sci. Lett.*, *192*, 145–157.
Edwards, A. N., and J. M. N. T. Gray (2015), Erosion–deposition waves in shallow granular free-surface flows, *J. Fluid Mech.*, *762*, 35–67.
Edwards, A. N., S. Viroulet, B. P. Kokelaar, and J. M. N. T. Gray (2017), Formation of levees, troughs and elevated channels by avalanches on erodible slopes, *J. Fluid Mech.*, *823*, 278–315.
Fassett, C. I., and B. J. Thomson (2014), Crater degradation on the lunar maria: Topographic diffusion and the rate of erosion on the Moon, *J. Geophys. Res.: Planets*, *119*, 2169–9100, doi:10.1002/2014JE004698.
Felix, G., and N. Thomas (2004), Relation between dry granular flow regimes and morphology of deposits: Formation of levees in pyroclastic deposits, *Earth Planet. Sci. Lett.*, *221*, 197–213.
Forterre, Y. (2006), Kapiza waves as a test for three-dimensional granular flow rheology, *J. Fluid Mech.*, *563*, 123–132.
Forterre, Y., and O. Pouliquen (2003), Long-surface-wave instability in dense granular flows, *J. Fluid Mech.*, *486*, 21–50.
Frank, F., B. W. McArdell, C. Huggel, and A. Vieli (2015), The importance of entrainment and bulking on debris flow runout modeling: Examples from the Swiss Alps, *Nat. Hazards Earth Syst. Sci.*, *15*, 2569–2583.
Freeman, V. L. (1981), Regolith of the Apollo 16 site, in *Geology of the Apollo 16 Area, Central Lunar Highlands*, *United States Geol. Surv. Prof. Pap*, vol. 1048, edited by G. E. Ulrich, C. A. Hodges, and W. R. Muehlberger, pp. 147–159 , US Government Printing Office, Washington.
GDR Midi (2004), On dense granular flows, *Eur. Phys. J. E: Soft Matter Biol. Phys.*, *14*, 341–365.
Ghent, R. R., P. O. Hayne, J. L. Bandfield, B. A. Campbell, C. C. Allen, L. M. Carter, and D. A. Paige (2014), Constraints on the recent rate of lunar ejecta breakdown and implications for crater ages, *Geology*, *42*, 1059–1062.
Gray, J. M. N. T., and C. Ancey (2009), Segregation, recirculation and deposition of coarse particles near two-dimensional avalanche fronts, *J. Fluid Mech.*, *629*, 387–423.
Gray, J. M. N. T., and C. Ancey (2011), Multi-component particle size-segregation in shallow granular avalanches, *J. Fluid Mech.*, *678*, 535–588.
Gray, J. M. N. T., and C. Ancey (2015), Particle-size and -density segregation in granular free-surface flows, *J. Fluid Mech.*, *779*, 622–668.
Gray, J. M. N. T., and V. A. Chugunov (2006), Particle-size segregation and diffusive remixing in shallow granular avalanches, *J. Fluid Mech.*, *569*, 365–398.
Gray, J. M. N. T., and A. N. Edwards (2014), A depth-averaged $\mu(I)$-rheology for shallow granular free-surface flows, *J. Fluid Mech.*, *755*, 503–534.
Gray, J. M. N. T., and B. P. Kokelaar (2010), Large particle segregation, transport and accumulation in granular free-surface flows, *J. Fluid Mech.*, *652*, 105–137.
Gray, J. M. N. T., and A. R. Thornton (2005), A theory for particle size segregation in shallow granular free-surface flows, *Proc. R. Soc. A*, *461*, 1447–1473.
Gray, J. M. N. T., M. Wieland, and K. Hutter (1999), Free surface flow of cohesionless granular avalanches over complex basal topography, *Proc. R. Soc. A*, *455*, 1841–1874.
Hawke, B. R., C. R. Coombs, B. A. Campbell, P. G. Lucey, C. A. Peterson, and S. H. Zisk (1991), Remote sensing of regional pyroclastic deposits on the north central portion of the lunar nearside, *Proc. Lunar Planet. Sci.*, *21*, 377–389.
Hiesinger, H., and J. W. Head III (2006), New views of lunar geoscience: An introduction and overview, *Rev. Mineral. Geochem.*, *60*, 1–81.
Hiesinger, H., R. Jaumann, G. Neukum, and J. W. Head III (2000), Ages of mare basalts on the lunar nearside, *J. Geophys. Res.*, *105*, 29,239–29,275, doi:10.1029/2000JE001244.
Hörz, F., R. Grieve, G. Heiken, P. Spudis, and A. Binder (1991), Lunar surface processes, in *Lunar Sourcebook*, edited by G. Heiken, D. Vaniman, and B. M. French, pp. 61–120, Cambridge Univ. Press, Cambridge.
Hörz, F., J. B. Hartung, and D. E. Gault (1971), Micrometeorite craters on lunar rock surfaces, *J. Geophys. Res.*, *76*, 5770–5798, doi:10.1029/JB076i023p05770.
Houston, W. N., Y. Moriwaki, and C.-S. Chang (1973), Downslope movement of lunar soil and rock caused by meteoroid impact, Proc. of the 4th Lunar Sci. Conf., 2425–2435.
Howard, K. A. (1973), Avalanche mode of motion: Implications from lunar examples, *Science*, *180*, 1052–1055.
Hsü, K. J. (1975), Catastrophic debris streams (sturzstroms) generated by rockfalls, *Geol. Soc. Am. Bull.*, *86*, 129–140.
Hurwitz, D., and D. A. Kring (2016), Identifying the geologic context of Apollo 17 impact melt breccias, *Earth Planet. Sci. Lett.*, *436*, 64–70.
Iverson, R. M. (1997), The physics of debris flows, *Rev. Geophys.*, *35*, 245–296, doi:10.1029/97RG00426.
Iverson, R. M., M. E. Reid, M. Logan, R. G. LaHusen, J. W. Godt, and J. G. Griswold (2011), Positive feedback and momentum growth during debris-flow entrainment of wet bed sediment, *Nat. Geosci.*, *4*, 116–121.
Izvekova, Y. N., and S. W. I. Popel (2013), Adhesion of rough particles of lunar regolith, *EPSC Abstr.*, *8*, 1–2.
Jain, S. (2014), *Weathering and Mass Wasting, Fundamentals of Physical Geology*, *Springer Geol.*, pp. 129–163, Springer, India.

Johnson, B. C., C. S. Campbell, and H. J. Melosh (2016), Reply to comment by Iverson on "The reduction of friction in long runout landslides as an emergent phenomenon", *J. Geophys. Res. Earth*, *121*, 2243–2246, doi:10.1002/2016JF004093.
Johnson, C. G., B. P. Kokelaar, R. M. Iverson, M. Logan, R. G. LaHusen, and J. M. N. T. Gray (2012), Grain-size segregation and levee formation in geophysical mass flows, *J. Geophys. Res.*, *117*, F01032, doi:10.1029/2011JF002185.
Jolliff, B. L., J. J. Gillis, L. A. Haskin, R. L. Korotev, and M. A. Wieczorek (2000), Major lunar crustal terranes: Surface expressions and crust-mantle origins, *J. Geophys. Res.*, *105*, 4197–4216, doi:10.1029/1999JE001103.
Jop, P., Y. Forterre, and O. Pouliquen (2006), A constitutive law for dense granular flows, *Nature*, *441*, 727–730.
Joy, K. H., I. A. Crawford, N. A. Curran, M. E. Zolensky, A. L. Fagan, and D. A. Kring (2016), The Moon as an archive of small body migration in the solar system, *Earth Moon Planet.*, *118*, 133, doi:10.1007/s11038-016-9495-0.
Kickapoo Lunar Research Team, and G. Kramer (2014), Stratified ejecta boulders as indicators of layered plutons on the Moon, *Icarus*, *228*, 141–148.
Kim, B. C., and D. R. Lowe (2004), Depositional processes of the gravelly debris flow deposits, South Dolomite alluvial fan, Owens Valley, California, *Geosci. J.*, *8*, 153–170.
Kleinhans, M. G., H. Markies, S. J. de Vet, A. C. In't Veld, and F. N. Postema (2011), Static and dynamic angles of repose in loose granular materials under reduced gravity, *J. Geophys. Res.*, *116*, E11004, doi:10.1029/2011JE003865.
Köhler, A., J. N. McElwaine, B. Sovilla, M. Ash, and P. Brennan (2016), The dynamics of surges in the 3 February avalanches in Vallée de la Sionne, *J. Geophys. Res. Earth*, *121*, 2192–2210, doi:10.1002/2016JF003887.
Kokelaar, B. P., R. L. Graham, J. M. N. T. Gray, and J. W. Vallance (2014), Fine-grained linings of leveed channels facilitate runout of granular flows, *Earth Planet. Sci. Lett.*, *385*, 172–180.
Kreslavsky, M. A., and J. W. Head III (2016), The steepest slopes on the Moon from Lunar Orbiter Laser Altimeter (LOLA) data: Spatial distribution and correlation with geologic features, *Icarus*, *273*, 329–336.
Krohn, K., et al. (2014), Mass movement on Vesta at steep scarps and crater rims, *Icarus*, *244*, 120–132.
Kumar, P. S., V. Keerthi, A. S. Kumar, J. Mustard, B. G. Krishna, L. R. Ostrach, D. A. Kring, A. S. K. Kumar, and J. N. Goswami (2013), Gullies and landslides on the Moon: Evidence for dry-granular flows, *J. Geophys. Res.: Planets*, *118*, 206–223, doi:10.1002/jgre.20043.
Kumar, P. S., U. Sruthi, N. Krishna, K. J. P. Lakshmi, R. Menon, B. Gopala Krishna, D. A. Kring, J. W. Head, J. N. Goswami, and A. S. Kiran Kumar (2016), Recent shallow moonquake and impact-triggered boulder falls on the Moon: New insights from the Schrödinger basin, *J. Geophys. Res.: Planets*, *121*, 147–179, doi:10.1002/2015JE004850.
Langevin, Y., and J. R. Arnold (1977), The evolution of the lunar regolith, *Annu. Rev. Earth Planet. Sci.*, *5*, 449–489.
Legros, F. (2002), The mobility of long-runout landslides, *Eng. Geol.*, *63*, 301–331.
Lube, G., S. J. Cronin, T. Platz, A. Freundt, J. N. Proctor, C. Henderson, and M. F. Sheridan (2007), Flow and deposition of pyroclastic granular flow: A type example from the 1975 Ngauruhoe eruption, New Zealand, *J. Volcanol. Geotherm. Res.*, *161*, 165–186.
Lucey, P., et al. (2006), New views of the Moon: Understanding the lunar surface and space-Moon interactions, *Rev. Mineral. Geochem.*, *60*, 83–219.
Mangeney, A., O. Roche, O. Hungr, N. Mangold, G. Faccanoni, and A. Lucas (2010), Erosion and mobility in granular collapse over sloping beds, *J. Geophys. Res.*, *115*, F03040, doi:10.1029/2009JF001462.
McCubbin, F. M., et al. (2015), Magmatic volatiles (H, C, N, F, S, Cl) in the lunar mantle, crust, and regolith: Abundances, distributions, processes, and reservoirs, *Am. Mineral.*, *100*, 1668–1707.
McEwen, A. S., C. M. Dundas, S. S. Mattson, A. D. Toigo, L. Ojha, J. J. Wray, M. Chojnacki, S. Byrne, S. L. Murchie, and N. Thomas (2014), Recurring slope lineae in equatorial regions of Mars, *Nat. Geosci.*, *7*, 53–58.
McKay, D. S., R. M. Fruland, and G. H. Heiken (1974), Grain size and the evolution of lunar soils, *Proc. 5th Lunar Sci. Conf.*, *1*, 887–906.
McKay, D. S., G. Heiken, A. Basu, G. Blanford, S. Simon, R. Reedy, B. M. French, and J. Papike (1991), The lunar regolith, in *Lunar Sourcebook*, edited by G. Heiken, D. Vaniman, and B. M. French, pp. 286–356 , Cambridge Univ. Press, Cambridge.
Megens, M., and J. Aizenberg (2003), Capillary attraction: Like-charged particles at liquid interfaces, *Nature*, *424*, 1040.
Melosh, H. J. (1979), Acoustic fluidization: A new geologic process? *J. Geophys. Res.*, *84*, 7513–7520, doi:10.1029/JB084iB13p07513.
Melosh, H. J. (1984), Impact ejection, spallation, and the origin of meteorites, *Icarus*, *59*, 234–260.
Melosh, H. J. (1986), The mechanics of large rock avalanches, *Rev. Eng. Geol.*, *7*, 41–50.
Melosh, H. J., and B. A. Ivanov (1999), Impact crater collapse, *Annu. Rev. Earth Planet. Sci.*, *27*, 385–415.
Mendell, W. W., and F. J. Low (1974), Preliminary results of the Apollo 17 infrared scanning radiometer, *Moon*, *9*, 97–103, doi:10.1007/BF00565396.
Mendell, W. W., and F. J. Low (1975), Infrared orbital mapping of lunar features, Proc. of 6th Lunar Sci. Conf., 2711–2719.
Meyer, C. (2011), Lunar 12062, Ilmenite Basalt, Lunar Sample Compendium, 1–4.
Molaro, J., and S. Byrne (2012), Rates of temperature change of airless landscapes and implications for thermal stress weathering, *J. Geophys. Res.*, *117*, E10011, doi:10.1029/2012JE004138.
Molaro, J. L., S. Byrne, and J. L. Le (2017), Thermally induced stresses in boulders on airless body surfaces, and implications for rock breakdown, *Icarus*, doi:10.1016/j.icarus.2017.03.008.
Moore, H. J., J. M. Boyce, G. G. Schaber, and D. H. Scott (1980), Lunar remote sensing and measurements, in *Apollo 15–17 Orbital Investigations*, *U.S. Geol. Surv. Prof. Pap.*, vol. 1046-B, p. 78, U.S. Gov. Print. Off., Washington, D. C.
Moore, J. G., W. R. Normark, and R. T. Holcomb (1994), Giant Hawaiian landslides, *Annu. Rev. Earth Planet. Sci.*, *22*, 119–144.
National Research Council (NRC) (2007), *Report on the Scientific Context for the Exploration of the Moon. Committee on the Scientific Context for Exploration of the Moon Space Studies Board Division on Engineering and Physical Sciences*, p. 120 , The National Academies Press, Washington.
Oberbeck, V. R., R. H. Morrison, and F. Hörz (1975), Transport and emplacement of crater and basin deposits, *Moon*, *13*, 9–26.
Oberbeck, V. R., and W. L. Quaide (1968), Genetic implications of lunar regolith thickness variations, *Icarus*, *9*, 446–465.
Öhman, T., and D. A. Kring (2012), Photogeologic analysis of impact melt-rich lithologies in Kepler crater that could be sampled by future missions, *J. Geophys. Res.*, *117*, E00H08, doi:10.1029/2011JE003918.
Otto, K. A., R. Jaumann, K. Krohn, F. Preusker, T. Roatsch, K. Stephan, M. V. Sykes, P. Schenk, C. A. Raymond, and C. T. Russell (2013), Mass wasting processes in Vesta's south polar region Rheasilvia, *J. Geophys. Res.: Planets*, *118*, 2279–2294, doi:10.1002/2013JE004333.
Pajola, M., et al. (2017), Pristine interior of comet 67P revealed by the combined Aswan outburst and cliff collapse, *Nat. Astron.*, *1*, 0092.
Parker, R. N., A. L. Densmore, N. J. Rosser, M. de Michele, Y. Li, R. Huang, S. Whadcoat, and D. N. Petley (2011), Mass wasting triggered by the 2008 Wenchuan earthquake is greater than orogenic growth, *Nat. Geosci.*, *4*, 449–452.
Pernet-Fisher, J. F., and K. H. Joy (2016), The lunar highlands: Old crust, new ideas, *Astron. Geophys.*, *57*, 1.26–1.30.
Petro, N. E., and C. M. Pieters (2008), The lunar-wide effects of basin ejecta distribution on the early megaregolith, *Meteorit. Planet. Sci.*, *43*, 1517–1529.

Pike, R. J. (1967), Schroeter's rule and the modification of lunar crater impact morphology, *J. Geophys. Res.*, *72*, 2099–2106, doi:10.1029/JZ072i008p02099.
Pike, R. J. (1971), Some preliminary interpretations of lunar mass-wasting process from Apollo 10 photography, in *Analysis of Apollo 10 Photography and Visual Observations*, pp. 14–20, NASA SP-232, Washington, D. C.
Pitcher, C., N. Kömle, O. Leibniz, O. Morales-Calderon, Y. Gao, and L. Richter (2016), Investigation of the properties of icy lunar polar regolith simulants, *Adv. Space Res.*, *57*, 1197–1208.
Pohlman, N., B. Severson, J. Ottino, and R. Lueptow (2006), Surface roughness effects in granular matter: Influence on angle of repose and absence of segregation, *Phys. Rev. E*, *73* 031304.
Popel, S. I., S. I. Kopnin, A. P. Golub, G. G. Dol'nikov, A. V. Zakharov, L. M. Zelenyi, and Y. N. Izvekova (2013), Dusty plasma at the surface of the Moon, *Sol. Syst. Res.*, *47*, 419–429.
Potts, N. J., A. L. Gullikson, N. M. Curran, J. K. Dhaliwal, M. K. Leader, R. N. Rege, K. K. Klaus, and D. A. Kring (2015), Robotic traverse and sample return strategies for a lunar farside mission to the Schrödinger basin, *Adv. Space Res.*, *55*, 1241–1254.
Pouliquen, O. (1999), Scaling laws in granular flows down rough inclined planes, *Phys. Fluids*, *11*, 542–548.
Pouliquen, O., J. Delour, and S. B. Savage (1997), Fingering in granular flows, *Nature*, *386*, 816–817.
Pouliquen, O., and Y. Forterre (2002), Friction law for dense granular flows: Application to the motion of a mass down a rough inclined plane, *J. Fluid Mech.*, *453*, 133–151.
Pouliquen, O., and J. W. Vallance (1999), Segregation induced instabilities of granular fronts, *Chaos*, *9*, 621–630.
Quaide, W. L., and V. R. Oberbeck (1975), Development of the mare regolith: Some model considerations, *Moon*, *13*, 27–55.
Razis, D., A. N. Edwards, J. M. N. T. Gray, and K. van der Weele (2014), Arrested coarsening of granular roll waves, *Phys. Fluids*, *26*, 297–329.
Robinson, M. S., and B. L. Jolliff (2002), Apollo 17 landing site: Topography, photometric corrections, and heterogeneity of the surrounding highland massifs, *J. Geophys. Res.*, *107*(E11), 5110, doi:10.1029/2001JE001614.
Robinson, M. S., et al. (2010), Lunar Reconnaissance Orbiter Camera (LROC) instrument overview, *Space Sci. Rev.*, *150*, 81–124.
Savage, S. B., and K. Hutter (1989), The motion of a finite mass of granular material down a rough incline, *J. Fluid Mech.*, *199*, 177–215.
Savage, S. B., and C. K. K. Lun (1988), Particle size segregation in inclined chute flow of dry cohesionless granular solids, *J. Fluid Mech.*, *189*, 311–335.
Schmidt, F., F. Andrieu, F. Costard, M. Kocifaj, and A. G. Meresescu (2017), Formation of recurring slope lineae on Mars by rarefied gas-triggered granular flows, *Nat. Geosci.*, doi:10.1038/NGEO2917.
Schmitt, H. H., N. E. Petro, R. A. Wells, M. S. Robinson, B. P. Weiss, and C. M. Mercer (2017), Revisiting the field geology of Taurus-Littrow, *Icarus*, doi:10.1016/j.icarus.2016.11.042.
Schultz, P. H., and D. E. Gault (1976), Seismically induced modification of lunar surface features, Proc. of 6th Lunar Sci. Conf., 2845–2862.
Shorthill, R. W. (1970), Infrared Moon—A review, *J. Spacecr. Rocket.*, *7*, 385–397.
Soderblom, L. A. (1970), A model for small-impact erosion applied to the lunar surface, *J. Geophys. Res.*, *75*, 2655–2661, doi:10.1029/JB075i014p02655.
Smith, D. E., et al. (2010), Initial observations from the Lunar Orbiter Laser Altimeter (LOLA), *Geophys. Res. Lett.*, *37*, L18204, doi:10.1029/2010GL043751.
Spray, J. G. (2016), Lithification mechanisms for planetary regoliths: The glue that binds, *Annu. Rev. Earth Planet. Sci.*, *44*, 139–174.
Spudis, P. D., D. B. J. Bussey, S. M. Baloga, J. T. S. Cahill, L. S. Glaze, G. W. Patterson, R. K. Raney, T. W. Thompson, B. J. Thomson, and E. A. Ustinov (2013), Evidence for water ice on the Moon: Results for anomalous polar craters from the LRO Mini-RF imaging radar, *J. Geophys. Res.: Planets*, *118*, 2016–2029, doi:10.1002/jgre.20156.
Steenstra, E. S., et al. (2016), Analyses of robotic traverses and sample sites in the Schrödinger basin for the HERACLES human-assisted sample return mission concept, *Adv. Space Res.*, *58*, 1050–1065.
Stöffler, D., G. Ryder, B. A. Ivanov, N. A. Artemieva, M. J. Cintala, and R. A. F. Grieve (2006), Cratering history and lunar chronology, in new views of the Moon, *Rev. Mineral. Geochem.*, *60*, 519–596.
Sullivan, R., P. Thomas, J. Veverka, M. Malin, and K. S. Edgett (2001), Mass movement slope streaks imaged by the Mars orbiter camera, *J. Geophys. Res.*, *106*, 23,607–23,633, doi:10.1029/2000JE001296.
Takahashi, T., H. Nakagawa, T. Harada, and Y. Yamashiki (1992), Routing debris flows with particle segregation, *J. Hydraul. Eng.*, *118*, 1490–1507.
Train, D. (1958), Some aspects of the property of angle of repose of powders, *J. Pharm. Pharmacol.*, *10*, 127T–135T.
Tran, T., et al. (2010), Generating digital terrain models using LROC NAC images, Commission VI, WG VI/4, 1-7.
Treiman, A. H. (2003), Geologic settings of Martian gullies: Implications for their origins, *J. Geophys. Res.*, *108*(E4), 8031, doi:10.1029/2002JE001900.
Vallance, J. W., and S. B. Savage (2000), Particle segregation in granular flows down chutes, in *IUATM Symposium on Segregation in Granular Flows*, edited by A. D. Rosato and D. L. Blackmore, pp. 31–52, Kluwer Acad., Boston, Mass.
Varnes, D. J. (1978), Slope movement types and processes, in *Landslides, Analysis and Control*, *Transportation Research Board Sp. Rep*, vol. 176, edited by R. L. Schuster and R. J. Krizek, pp. 11–33, Nat. Acad. of Sciences, Washington, D. C.
Viroulet, S., J. L. Baker, A. N. Edwards, C. G. Johnson, C. Gjaltema, P. Clavel, and J. M. N. T. Gray (2017), Multiple solutions for granular flow over a smooth two-dimensional bump, *J. Fluid Mech.*, *815*, 77–116.
Wagner, R. V., M. S. Robinson, E. J. Speyerer, and P. Mahanti (2013), Topography of 20-km diameter craters on the Moon. 44th Lunar and Planet. Sci. Conf., Abstract, 2924.
Watters, T. R., M. S. Robinson, M. E. Banks, T. Tran, and B. W. Denevi (2012), Recent extensional tectonics on the Moon revealed by the Lunar Reconnaissance Orbiter Camera, *Nat. Geosci.*, *5*, 181–185.
Wilcox, B. B., M. S. Robinson, P. C. Thomas, and B. R. Hawke (2005), Constraints on the depth and variability of the lunar regolith, *Meteorit. Planet. Sci.*, *40*, 695–710.
Wilhelms, D. E. (1987), Professional papers 1348, *Geol. History Moon*, 57–81.
Williams, D. A., et al. (2014), Lobate and flow-like features on asteroid Vesta, *Planet. Space Sci.*, *103*, 24–35.
Wolman, M. G., and R. Gerson (2007), Relative scales of time and effectiveness of climate in watershed geomorphology, *Earth Surf. Processes*, *3*, 189–208.
Woodhouse, M. J., A. R. Thornton, C. G. Johnson, B. P. Kokelaar, and J. M. N. T. Gray (2012), Segregation-induced fingering instabilities in granular free-surface flows, *J. Fluid Mech.*, *709*, 543–580.
Xiao, Z., Z. Zeng, N. Ding, and J. Molaro (2013), Mass wasting features on the Moon—How active is the lunar surface?, *Earth Planet. Sci. Lett.*, *376*, 1–11.
Zhou, Y. C., B. H. Xu, A. B. Yu, and P. Zulli (2002), An experimental and numerical study of the angle of repose of coarse spheres, *Power Tech.*, *125*, 45–54.